DEVELOPMENT OF A SEMI-ANALYTICAL MODEL FOR SEAGRASS MAPPING USING CLOUD-BASED COMPUTING AND OPEN SOURCED OPTICAL SATELLITE DATA

CHENGFA BENJAMIN LEE

A thesis submitted to the
Julius-Maximilians-Universität Würzburg
in partial fulfilment for the
Degree of Master of Science
in
Applied Earth observation & Geoanalysis of the Living Environment (EAGLE)

Department of Remote Sensing, Julius-Maximilians-Universität Würzburg
in collaboration with
Remote Sensing Technology Institute (IMF),
Earth Observation Center, German Aerospace Center (DLR-EOC)

First Supervisor : Dr. Christian Hüttich
Second Supervisor : Dr. Peter Reinartz

2020

Declaration

I hereby declare that this thesis is my original work and it has been written by me in its entirety. I have duly acknowledged all the sources of information which have been used in the thesis.

This thesis has also not been submitted for any degree in any university previously.

_____

Lee, Chengfa Benjamin

6 March 2020

Acknowledgement

I wish to thank Dr. Christian Hüttich, Dr. Peter Reinartz and Dimosthenis Traganos for their guidance throughout this project. Special mention is due to Magdalena Main-Knorn, Bringfried Pflug and Spyrodon Christofilakos, who have made direct contributions to this study. I am also grateful for the assistance and hospitality provided to me by all members of the IMF Berlin-Adlershof department.

I would like to acknowledge Dimosthenis Traganos, Dimitris Poursanidis and Aurelie Shapiro for spearheading the East Africa Seascape Mapping in the Cloud project, which this thesis is a component of. I am also much indebted to the World Wide Fund for Nature and their local, Mozambican volunteers for collecting and sharing the ground bathymetry data for Quirimbas National Park.

In addition to my supervisors and mentor, I greatly appreciate the help rendered to my thesis in one way or another by Johni Miah, Tan Liuyi Jan, Maninder Singh Dhillon, Silvan Balthasar Steiner and Yee Qing Xiang.

Recognition is due to Felix Glasmann, whose internship at the EOMAP GmbH & Co. KG inspired me to search for a topic pertaining to my interests in the coastal, intertidal and subtidal research field. Marius Balthasar Philipp also provided invaluable aid for my relocation to Berlin.

Finally, I am glad for all the support and understanding from my family, close friends and fellow classmates.

The East Africa Seascape Mapping in the Cloud project is funded by the INT/OCEANS INNOVATION FUNDS, Project Number: 10004197 / 20145371/745.

Table of Contents

Abstract

Seagrasses provide USD$2.28 trillion in annual ecosystem services, with US$169 million arising solely from blue carbon sequestration, the absorption and storage of carbon emissions from these coastal vegetated ecosystems. Unfortunately, 51,000 km^2 or 29% of the known global seagrasses were lost between 1879 and 2006. The best global seagrass map is an assemblage of known areas since the 1930s. With growing interests in blue carbon, a standardised approach to map seagrass is needed. Aquatic remote sensing introduces the water column as a second medium and other aquatic-specific challenges. Solutions include the computationally expensive physics-based or analytical approach, which is less data-dependent than the conventional statistical approach, or the hybrid semi-analytical approach which combines the strengths of both. Fortunately, the advent of cloud computing services such as the Google Earth Engine (GEE) brings easy access to computational power. This study aims to implement a semi-analytical approach on GEE to map seagrasses in Mozambique. A forward Hyperspectral Optimisation Process Exemplar (HOPE) model based on Sentinel-2 was implemented and supplemented by a bathymetry log-linear regression and published intrinsic optical properties of water (IOPs) values and/or equations. Support Vector Machine and Random Forest were used for classification. Support Vector Machine produced the best areal estimate of 3518.37 km^2 with a seagrass producer's accuracy of 51.02%, a seagrass user's accuracy of 65.79% and an overall accuracy of 60.27%. The best bathymetry estimate featured an R^2 of 0.68. Although there was no validation for IOPs, external validation showed that the total absorption had less than 25% difference from the Case-2 Regional / Coast Colour (C2RCC) processor. While requiring further improvements, this model has shown potential for seagrass mapping, especially in remote or understudied regions, and is a step towards a global seagrass map.

(287 words)

Keywords: Seagrass, Distribution map, Mozambique, Google Earth Engine, HOPE, semi-analytical, Sentinel-2, cloud computing

List of Figures

List of Tables

List of Abbreviations & Symbols

ALOS	Advanced Land Observing Satellite
AOP	Apparent optical property of water
AWS	Amazon Web Services
a_{tot}	Total absorption coefficient
BRUCE	Bottom Reflectance Unmixing Computation of the Environment
b	Total backscatter coefficient
C2RCC	Case-2 Regional / Coast Colour
DII	Depth Invariant Index
DN	Digital number
DSM	Digital surface model
DOS	Dark Object Subtraction
GEBCO	General Bathymetric Chart of the Oceans
GEE	Google Earth Engine
HOPE	Hyperspectral Optimisation Process Exemplar
ICESat-2	Ice, Cloud, and Land Elevation Satellite-2
IOP	Intrinsic optical property of water
LiDAR	Light Detection and Ranging
K	Attenuation coefficient
L_u	Reflectance value of upwelling light
MODIS	Moderate-resolution Imaging Spectroradiometer
NDWI	Normalised Difference Water Index
NIR	Near-infrared
NOAA	National Oceanic and Atmospheric Administration
PA	Producer's accuracy
PRISM	Portable Remote Imaging SpectroMeter
QNP	Quirimbas National Park
RF	Random Forest
RMSE	Root Mean Square error

R_{raw}	Raw sea surface reflectance
R_{rhown}	Above water normalised reflectance
R_{rs}	Water surface reflectance
r_{rs}	Sub-surface or below water surface reflectance
r_{rs}^{b}	Bottom reflectance
r_{rs}^{dp}	Sub-surface reflectance in deep waters
SAMBUCA	Semi-analytical Model for Bathymetry, Unmixing, and Concentration Assessment
SDB	Satellite-derived Bathymetry
SRTM	Shuttle Radar Topography Mission
SVM	Support Vector Machine
SWIR	Shortwave Infrared
UA	User's accuracy
WWF	World Wide Fund for Nature
λ	Wavelength
θ_v	Satellite viewing angle
θ_w	Solar zenith angle
ρ	Bottom reflectance

1. Introduction

1.1. Seagrass meadows – an inconspicuous habitat under threat

Seagrasses are aquatic flowering plants that grow in coastal and marine environments, providing as much as USD$2.28 trillion in ecosystem services annually (Davidson et al., 2019). Their so-called blue carbon sequestration service based on the storage of carbon dioxide in the form of plant matter was evaluated at almost US$169 million (Luisetti et al., 2013). They also trap and bind sediments, which reduces the sediment load in the water. This has a two-fold benefit of stabilising the bottom substrate as well as purifying the water (Duarte, 2002). In turn, these benefit the adjacent coral ecosystem which is deeper and therefore requires clearer waters for greater light penetration into water (Purvaja et al., 2018). Excess production is exported in the form of nutrients to the production deficit ecosystems such as coral reefs, which both helps with sustaining the adjacent ecosystem and further contributes to blue carbon storage beyond the seagrass meadows (Duarte & Cebrián, 1996). Seagrass meadows are also a habitat and nursery to many marine species, including those of high commercial value (Nordlund et al., 2016). Five of the top 25 most commercially fished species, including the top and sixth on the list, are reliant on healthy seagrass habitats, which also contribute to 20% of the global commercial fish production (Unsworth et al., 2019b). In the Mediterranean, this increases to 30–40% despite seagrass meadows constituting only less than 2% of its cover (Jackson et al., 2015). As a primary producer, seagrasses are a food source for marine herbivores such as green turtles and the critically endangered dugong (Nakaoka & Aioi, 1999; Preen, 1995; Sheppard et al., 2007). Larger species of seagrasses do also provide a certain degree of wave attenuation which contributes to coastal protection (Duarte, 2002).

Unfortunately, seagrass habitats are under threat from many sources, both natural and anthropogenic. The most major threats are sedimentation and water pollution, such as waste water effluent or run-offs which reduces light penetration in water (Duffy et al., 2019; Fortes, 2018; Grech et al., 2012). Without light, the photosynthetic seagrasses are less likely to survive (Purvaja et al., 2018). Similarly, coastal eutrophication or algal blooms threaten seagrass through light obstruction (Purvaja et al., 2018). Meanwhile, coastal development threatens seagrass by either partially or fully replacing these seagrass meadows with urban structure (Fortes, 2018; Grech et al., 2012). Seagrasses are also affected by climate change and other environmental changes (Grech et al., 2012). A heatwave in 2011 directly resulted

in the loss of 22% of the seagrass meadows in Shark Bay, Australia, which led to a sharp decrease in water quality and a loss of at least 4 Mg C ha^{-1} in blue carbon stock within only a few years (Arias-Ortiz et al., 2018). On a local level, harmful fishing or boat practices, seaweed farming and even coral sand mining undermines seagrasses (Grech et al., 2012; Unsworth et al., 2019a, 2018).

While seagrasses have only recently started to recover in Europe (de los Santos et al., 2019), the global seagrass trend elsewhere is declining. Between 1879 and 2006, about 51,000 km^2 or 29% of the known global seagrass meadows were lost (Waycott et al., 2009). Despite their strong protection policies, Australia experienced a 2–40% loss in their monitoring sites between 2009 to 2014 (Evans et al., 2018). In regions where seagrasses have been understudied, such as Africa and Southeast Asia, any losses in seagrass meadows are unaccounted for (Fortes et al., 2018; Nordlund et al., 2016; Waycott et al., 2009). This poor data availability is a legacy issue, stemming from a history of scientific and funding neglect (Duarte et al., 2008; Unsworth et al., 2019a). Even now, the current best extent map of seagrass is an assemblage of known seagrass areas since the 1930s (UNEP-WCMC; Frederick T Short, 2017). With new seagrass meadows still being discovered in the last few years (Esteban et al., 2018; Tyllianakis et al., 2019), it is strongly indicative that there are still many knowledge gaps in basic information such as the global distribution of seagrasses.

Fortunately, the value of seagrass has gained international acknowledgement in recent years (Duffy et al., 2019). Many international organisations such as the Ramsar Convention on Wetlands have also begun to increase their efforts in seagrass research and conservation (Duffy et al., 2019). Still, most conservation programmes operate independently or are focused on only a small scale in space and time (Duffy et al., 2019). Even countries with a traditionally stronghold in seagrass research have yet to fully capitalise the strength of remote sensing to monitor seagrasses over large space and time (York et al., 2017). With the increased interests in national blue carbon stocks, it is thus necessary for a global standardised approach for seagrass mapping and monitoring (Traganos et al., 2018), to better index seagrass distribution (Duffy et al., 2019).

1.2. Applying remote sensing to seagrass research

With over a wide range of remote sensing methods such as hyperspectral and multispectral optical imagery, acoustics surveys and Light Detection and Ranging (LiDAR), remote sensing has contributed much to seagrass research (Hossain et al., 2015; Phinn et al., 2018). The freely available multispectral Landsat series and Sentinel-2 satellites have been a very popular choice for seagrass mapping (Dierssen et al., 2019; Kovacs et al., 2018; Topouzelis et al., 2018; Traganos et al., 2018; Yang & Yang, 2009). By integrating field photography with high spatial resolution optical images and *in-situ* above ground biomass data, Roelfsema et al. (2014) was able to map seagrass species and biomass over several time periods to obtain seagrass composition, biomass and their changes over time. Using a combination of optical imagery and a published model for post-disturbance soil carbon loss, Arias-Ortiz et al. (2018) was able to estimate the amount of seagrass and carbon stock over more than 10 years. Similarly, Yang & Yang (2009) created a model comparing semi-analytical model-derived Normalised Difference Vegetation Index (NDVI) values to the Leaf Area Index (LAI), which was then used to detect and monitor the seagrass meadows of Hainan, China, over 15 years. While such mid- to long-term studies are uncommon, they provide much spatial and/or temporal coverage that would have demanded a tremendous amount of labour and resources by conventional fieldwork to match the same coverage (Duffy et al., 2019). Poursanidis et al. (2019) have also explored the use of the Sentinel-2 coastal aerosol B1 band to detect subtidal seagrasses up to a depth of 32.2 m, which extends the possibility of mapping deeper seagrasses on a large scale using readily available optical imagery. Operating closer to the seagrass ecosystems, drones, aerial and sonar campaigns have also mapped seagrasses with great accuracy (Evans et al., 2018; Tyllianakis et al., 2019). Since seagrasses are not only found in clear waters, Dierssen et al. (2019) used the hyperspectral Portable Remote Imaging SpectroMeter (PRISM) to map seagrasses in turbid waters, which is much needed in many parts of the world. Beyond basic distribution maps, there were some successes in distinguishing between the various seagrass taxonomic groups using high-resolution multispectral optical imagery in Thailand (Koedsin et al., 2016) and Indonesia (Wicaksono et al., 2019; Wicaksono & Lazuardi, 2018); and both freely available and high-resolution multispectral optical imagery in Australia (Kovacs et al., 2018). With advances in satellite imaging technology such as sensors with better water penetrating bands as well as

hyperspectral satellites, remote sensing will continue to contribute in many new ways to seagrass research (Hossain et al., 2015).

While remote sensing contributes much, it has its limitations. There are many sources of freely available satellite images of various resolutions, such as the recent Sentinel-2 with a good spatial resolution of 10 m (Hossain et al., 2015; Kovacs et al., 2018; Phinn et al., 2018). As the better resolved images generally produces either more accurate outputs or have more diverse applications (Kovacs et al., 2018; Yang & Yang, 2009), depending on the needs of the study, one might be compelled to acquire their images from commercial sources such as the Worldview series images. Airborne images, LiDAR and aquatic sonar-based campaigns may also be used to acquire better resolved images, but such campaigns usually involve hefty costs and much more labour-intensive (Evans et al., 2018; Tyllianakis et al., 2019). Furthermore, all remote sensing approaches alike are susceptible to the effects of the environment, such as cloud, sun glint, turbidity or tides, which may either impair the quality of the optical-based images and consequently their outputs, or fully obscure the desired areas of interest (Kovacs et al., 2018; Phinn et al., 2018). While the standard course of action is to rely on non-optical, complementary approaches such as the selection of radar-based satellites to circumvent the issue of cloud or atmospheric obstruction as well as the sonar as the aquatic equivalent, the former do not penetrate into water and thus cannot be used to detect underwater objects while the latter is expensive as aforementioned (Hossain et al., 2015; Phinn et al., 2018). Another issue specific to aquatic remote sensing is the optical limit of light in deep waters, which is a physical limit that hampers the detection of deeper seagrasses (Poursanidis et al., 2019). While this might be resolved by adding sensors of specific wavelengths that have a good aquatic penetration to the satellites or airborne carrier, its successful application to seagrass detection will depend on the available selection of bands – both quantity and the choice of wavelengths (Hossain et al., 2015; Phinn et al., 2018).

Currently, there are many approaches to manage or mitigate such environmental and physical limitations, such as the plethora of correction methods available, the application of a multitemporal composite or a physics-based, analytical model (Hossain et al., 2015; Phinn et al., 2018). In particular, the analytical model attempts to account for various important parameters to correct for the effects of the atmosphere and water column to obtain the required reflectance values (Lee et al., 1998b). This reflectance output could then be used in

conjunction with a spectral library to identify the pixels without any validation data (Wicaksono & Lazuardi, 2018). However, these numerous calculations and calibrations to the local environment form a high barrier of entry for the analytical approach (Kerr & Purkis, 2018; Lee et al., 1998b). A compromise between these methods is the semi-analytical approach, which is based on the analytical approach but uses either approximation or statistical methods to substitute the much needed physical variables (Odermatt et al., 2012; Traganos & Reinartz, 2018). Furthermore, if ground truth data are available, conventional statistical classification can also be used on the derived reflectance values (Traganos & Reinartz, 2018).

Once the relevant and useful images are acquired, the next hurdle is the computational needs of data processing, especially if it is a large-scaled study that involves large number of images (Kerr & Purkis, 2018; Mutanga & Kumar, 2019). Such computational resources are uncommon and usually out of reach of many developing nations (Kumar & Mutanga, 2018) where the application of remote sensing to seagrass research is generally nascent (Duffy et al., 2019). The limited computational powers would only be further exacerbated should a physics-based model be used, as a popular calculation approach for such models is optimisation, which involves numerous iterations over each pixel to derive the best set of spectral values and is thus very computationally expensive (Gege, 2014; Kerr & Purkis, 2018).

With the advent of cloud computing, anyone is now able to have unprecedentedly easy access to powerful computer clusters, such as the online cloud computing platform Google Earth Engine (GEE), thereby having greater capabilities to map habitat on larger scales (Gorelick et al., 2017; Mutanga & Kumar, 2019). There are already several global scale surface land cover or habitat maps such as the intertidal areas (Murray et al., 2019). Naturally, the next goal is to implement a global scale map for seagrass habitats (Traganos & Reinartz, 2018). In order to achieve this goal, local scale studies are required to investigate and validate the seagrass mapping methods to be used for upscaling. Traganos et al. (2018) have implemented a conventional statistical-based approach on GEE to map the seagrasses of Greece, whose waters are characterised by a very narrow tidal range and generally clear waters. Naturally, such conditions are not found in many other parts of the world where seagrasses exist, and thus there is a need to design, scale and implement seagrass mapping methods that can be applied globally (Traganos & Reinartz, 2018).

1.3. Study Objectives

As part of a larger goal to account for national blue carbon stock in the East African region, this study aims to map the seagrasses in Mozambique. While there has been previous seagrass research in the Mozambican region (Bandeira et al., 2014; Green et al., 2003), the East African region has been historically a knowledge gap in seagrass research (Bandeira & Björk, 2001; Green et al., 2003). The paucity of ground truth data in this region has created difficulties for conventional statistical approaches which require auxiliary data for training and validation (Kerr & Purkis, 2018). However, data unavailability is not a barrier for analytical approaches, which only require the image spectral values for calculations (Odermatt et al., 2012). For the East African region, the hybrid semi-analytical method is a good compromise, as it provides the option to first test and calibrate the model to the region prior to its regional application. Given the information on Mozambican seagrass, this is an ideal natural laboratory to investigate use of the semi-analytical approach to map seagrass in East Africa.

Therefore, the aims of this study are:

(1) To implement a semi-analytical model to map seagrasses in Mozambique on the cloud computing GEE platform using Sentinel-2 imagery,
(2) To estimate the seagrass area in Mozambique,
(3) To obtain the intermediate Satellite-derived Bathymetry (SDB), the total optical absorption of water and bottom reflectance from the same model.

This thesis is structured into six chapters. Chapter 2 provides a literature review of the aquatic remote sensing theories and application relevant to this study, Chapter 3 introduces the study area and methodology, Chapter 4 reports the results, Chapter 5 elaborates on the discussion and Chapter 6 summarises the main findings in a conclusion.

2. Literature Review

2.1. Aquatic Remote Sensing

Since the seagrass meadow is an aquatic habitat, an aquatic remote sensing approach instead of the conventional terrestrial remote sensing is required. Owing to the lack of penetration by radar frequencies into water, aquatic remote sensing is largely dominated by optical sensors, sonar and LiDAR (Hossain et al., 2015). Besides the atmosphere, the aquatic medium has an additional influence of the water on light reflectance (Lee, Carder, Mobley, Steward, & Patch, 1998). Conventional empirical methods create a statistical relationship between the image spectral measurements and the training dataset without addressing any physical phenomenon such as the attenuation of light in water. Meanwhile, analytical methods derive the bottom reflectance through the radiative transfer theory, which involves modelling the simplified path of light from the source to the sensor and then trying to invert and deduce the values of all the variables based on the final spectral values of an image (Dekker et al., 2011; Odermatt et al., 2012; Phinn et al., 2018). While the former method has been used to map seagrasses (Traganos et al., 2018), its need for training data renders it less useful in areas without them, such as remote or understudied areas. The same restriction does not apply for the analytical approaches, as inversion relies only on the spectral values to deduce the values of the input variables (Kerr & Purkis, 2018).

2.2. Radiative Transfer Theory

Since the radiative transfer theory tries to account for the light path from source to sensor, there are two mediums to consider – air and water. The interaction of light in the air column is the same as conventional terrestrial remote sensing and thus will not be covered here. There are two other interactions, namely the interaction of light as it travels between air and water, and the interaction of light within the water column. Figure 1 illustrates these light interactions with the air and water medium, which will be further elaborated on in this section.

When light reaches the surface of a water body, most of the light will penetrate into the water, although some light is reflected off the water surface (Austin & Petzold, 1981). Depending on the position of the light source and the sensor, some of the reflected light may be directed at the sensor, resulting in light pollution known as sun glint (Phinn et al., 2018). Furthermore, light refracts when travelling between mediums of different densities, namely water and air,

further causing changes to the light path (Phinn et al., 2018). All these reducing effects on light that reaches the sensor is known as the diffuse attenuation coefficient (Austin & Petzold, 1981).

Once the light is underwater, the radiative theory assumes that the return signal from the water is a summation of signals from both the water column and the bottom (Lee et al., 1998a). During the process of travelling down to the bottom (downwelling) and back up through the water column (upwelling), light scattering and absorption occur causing attenuation or the loss of light energy (Lee et al., 1999). While there is a small amount of downwelling light backscattered in the direction of the sensor, it is not comparable to the loss of light energy from the attenuation of the upwelling light. Furthermore, the light reflected off the bottom is usually the dominant contribution to the light signal (Bostater & Rotkiske, 2018; Maritorena et al., 1994), which therefore allows for the bottom reflectance to be derived from a satellite image (Figure 2). The advantage of working with bottom reflectance rather than the other reflectance levels is that the bottom reflectance is the same globally and unaffected by local environmental conditions (Hochberg et al., 2003).

Since light attenuates exponentially as it travels further into the water, in waters that are sufficiently deep, light will be extinguished before it can complete its journey to the bottom

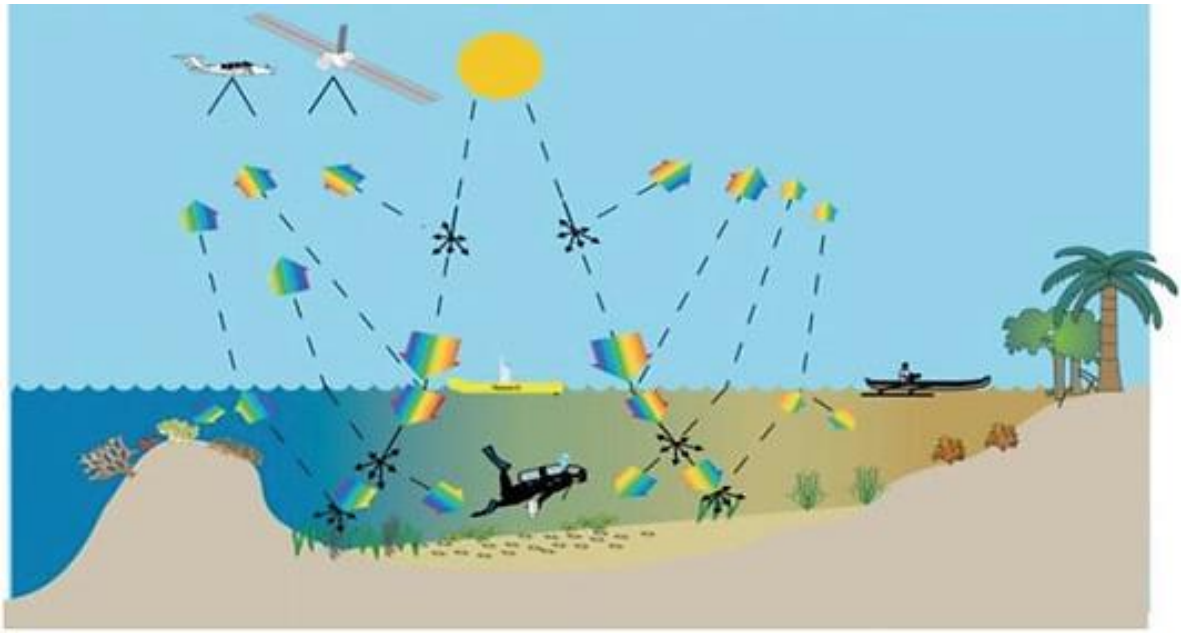

Figure 1. A simplified illustration of the light pathway and various sources of light loss when light travels to the bottom of the water body and then to the satellite sensor.
Image taken from Phinn et al. (2018).

and back, leading to a total absence of signal contribution from the bottom. Meanwhile, the backscattering of downwelling light from the water column still occurs, resulting in a low signal return. This is known as the optically deep water. While the bottom cover is no longer obtainable from these deep water pixels, useful water column information such as phytoplankton concentration and substrate suspension in the water column can still be derived (Lee et al., 2002, 1998b; Wei et al., 2019). Also, different wavelengths of light attenuate at different rates, thus have different penetration in the water column (Lyzenga, 1978), which can be exploited for purposes such as atmospheric correction (Siegel et al., 2000)

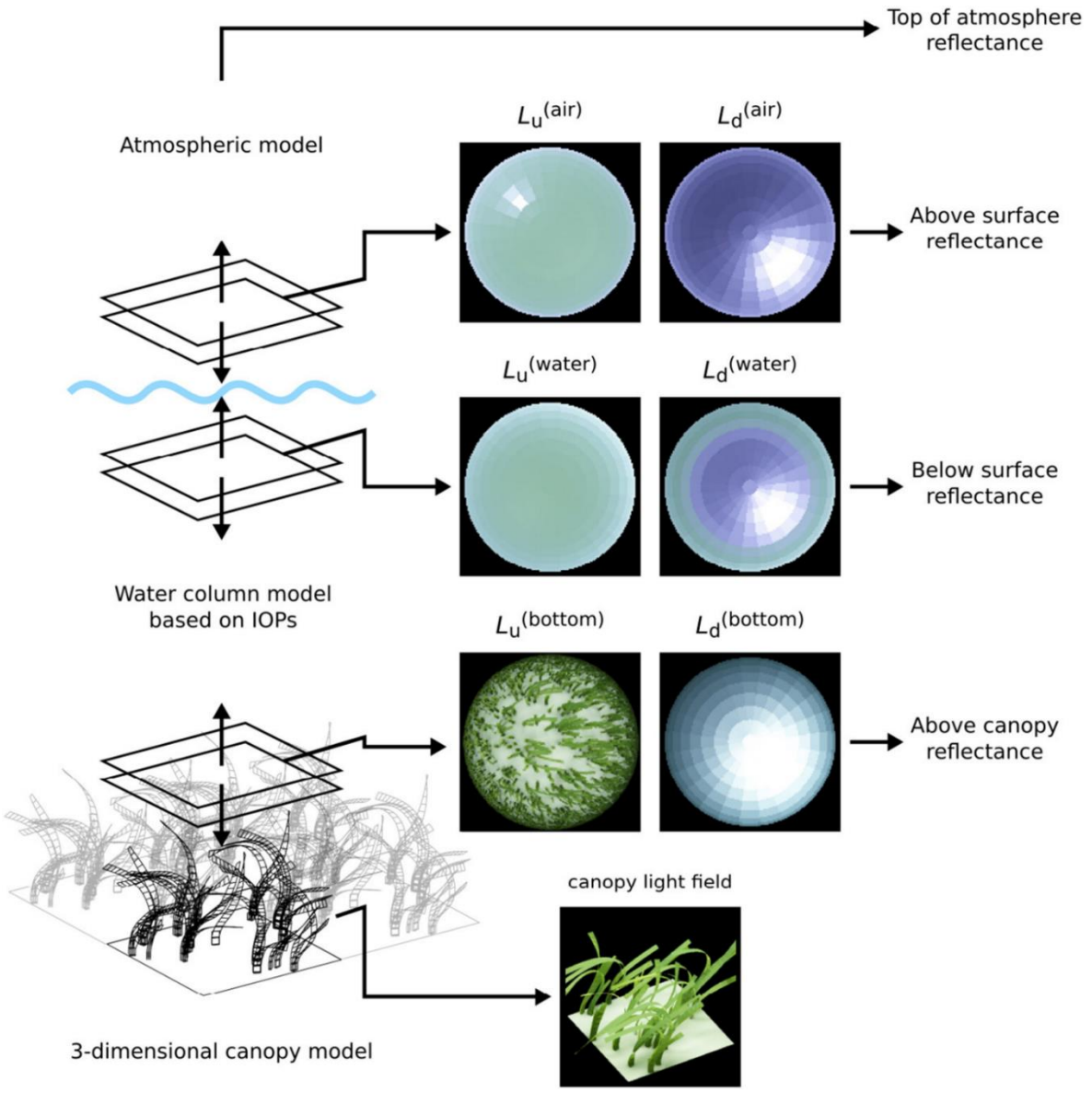

Figure 2. A stepwise illustration of how an analytical model would correct the upwelling reflectance values L_u recorded by the sensor, adapted from a scheme for a LiDAR sensor. Although the end product is a 3D model, this is conceptually applicable to a 2D image.
Image taken and adapted from Hedley et al. (2016).

and depth estimation (Lyzenga et al., 2006). As such, optically deep water pixels are the ideal location for performing sun glint corrections as well as disentangling the attenuation effects of the water and atmospheric columns, as there is a lack of bottom reflectance interfering with the calculations (Su & Huang, 2019).

Another factor that affects the light pathway underwater is the clarity or turbidity of the water. Suspended particles in water can generally be classified as phytoplankton, detritus or coloured dissolved organic materials (Sosik, 2008). These particles as well as the water molecules themselves will physically interact with the light and contribute to the intrinsic optical properties of water (IOP), which are the light-influencing properties of water that remains constant regardless of sensor angle (Kirk, 1984). Phytoplankton also absorb light energy for photosynthesis (Sosik, 2008), which further accelerate the extinction of light and limit the reception of bottom signals to shallower depths. Meanwhile, all particles contribute to a small amount of backscattering, so backscattering is increased in more turbid waters (Sosik, 2008). Furthermore, in severely turbid waters, the absorption and backscattering does not fit with the standard absorption and backscattering models (Whitlock et al., 1981).

When light travels from water to air *en route* to the sensor, some light is again reflected off the surface of the water downwards while the rest of the light is refracted again (Phinn et al., 2018). The remaining light is then under the effects of atmospheric attenuation before it reaches the sensor (Figure 1).

2.3. Application of the radiative theory to aquatic remote sensing

2.3.1. The pragmatic need for simplification

The radiative theory attempts to account for light-influencing variables in order to invert and calculate the bottom reflectance value from the final image spectral value, which can in turn be used to identify the bottom cover (Lee et al., 1999). In practice, there are too many variables for consideration and some of the variables require sophisticated measurements beyond current technological capabilities or highly complicated equations that would ironically deteriorate the inversion (Lee et al., 1998a). As such, it is necessary to simplify the models based on the radiative theory (Odermatt et al., 2012).

Much simplification was based on *ex-situ* spectrometer studies, which provided standard constants such as the absorption and backscatter of water particles (Austin & Petzold, 1981;

Bricaud et al., 1981; Morel, 1974; Zhang & Hu, 2009). Besides constants, simplification can be achieved by approximations based on empirical research (Lyzenga, 1981; Stumpf et al., 2003). This involves creating empirical constants and equations to describe the physical phenomenon, which will then be applied to another area by either assuming direct transferability of the equation(s) or recalibrating the model to the conditions of the new study site (Austin & Petzold, 1986; Lyzenga et al., 2006; Stumpf et al., 2003). To a lesser extent, this statistical approach is a small-scale empirical approach for acquiring the unknown variables. As such, its integration into an analytical model will produce a hybrid semi-analytical model (Kerr & Purkis, 2018). Finally, variables that contribute very little to the final outcome may be ignored or approximated into another variable (Lee et al., 1998a).

There are several analytical models for aquatic remote sensing. Initially developed using hyperspectral sensors to identify the important wavelengths (Lee et al., 1998a; Lyzenga, 1981), the analytical model has been adapted in recent years to the various free-to-use satellite sensors, such as Landsat and Sentinel-2 (Misra et al., 2018; Poursanidis et al., 2019). As many of the models originate from a few core literature (Lyzenga, 1981, 1978; Maritorena et al., 1994), the required input variables or parameters are generally similar across the various models, namely the absorption and backscatter IOPs, the depth of the water column and the bottom reflectance, as well as the image spectral measurements (Dekker et al., 2011). This study is based on the Hyperspectral Optimisation Process Exemplar model by Lee et al. (1999, 1998a).

2.3.2. Hyperspectral Optimisation Process Exemplar (HOPE) – a popular model for aquatic remote sensing

The Hyperspectral Optimisation Process Exemplar (HOPE) model is developed for deriving the various parameters in shallow waters, and based on the Hydrolight model (Brando et al., 2009; Lee et al., 2001). HOPE employs the inversion or optimisation method, which, given a set of input model equations and an error equation, uses a mathematical process that tries to minimise the output of the error equation while simultaneously fine-tuning the values of the input parameters to invert and identify the best set of parameters for the model (Brando et al., 2009; Lee et al., 1998a). For simpler equations, this method is usually very accurate. However, with greater complexities such as polynomial, logarithmic, or exponential equations, there might exist more than one mathematically sound set of parameters. In order to obtain

a physically realistic set of parameters, it is crucial to select reasonable starting values as well as optimisation hyperparameters. Optimisation is also computationally intensive as it will iterate over a pixel many times, thus may not be reasonably suited for larger spatial scales or if one does not have access to much computing power (Dekker et al., 2011; Kerr & Purkis, 2018).

Should one choose not to pursue the optimisation method, then the standard forward model has to be implemented. The input variables have to be derived separately in order to reduce the number of unknown variables in HOPE (Su & Huang, 2019). As the desired product is the bottom reflectance, the remaining unknown variables are the water depth and IOPs.

2.3.3. Using optical imagery to obtain bathymetry

Lyzenga (1981, 1978) proposed a log-linear model that capitalises on the constant but different rates of attenuation between wavelengths to create a relative depth index, known as the Depth Invariant Index (DII). As such, within the same bottom cover, the relationship between two logarithmic-transformed bands is linear, which can then be exploited to estimate the relative depths between points (Figure 3). Subsequently, the model can be calibrated with auxiliary bathymetry data, to calculate the true depth (Lyzenga et al., 2006). The drawback is that it is based on several assumptions which might be too basic and not reflective of the complex water column and thus many variants of these models have tried to rectify one or more of the basic assumptions (Figueiredo et al., 2016). For example, the band ratio model by Stumpf et al. (2003) is a non-linear approach that uses an empirically derived model to calibrate a band ratio equation to estimate water depth in an area (Caballero & Stumpf, 2019), while Figuerodo et al. (2016) tried to address the non-homogeneity of the water column's optical properties by integrating a regularisation theory into the model. Despite these various attempts to improve the basic model, Figuerodo et al. (2016) expressed uncertainty that their model would outperform the basic log-linear model in all situations, Su et al. (2008) found that similar overall performances between the linear and non-linear models despite non-linear models having slightly more accuracy. Given its simplicity and on-going relevance, the conventional log-linear model is a good pilot approach to deriving the bathymetry from optical imagery.

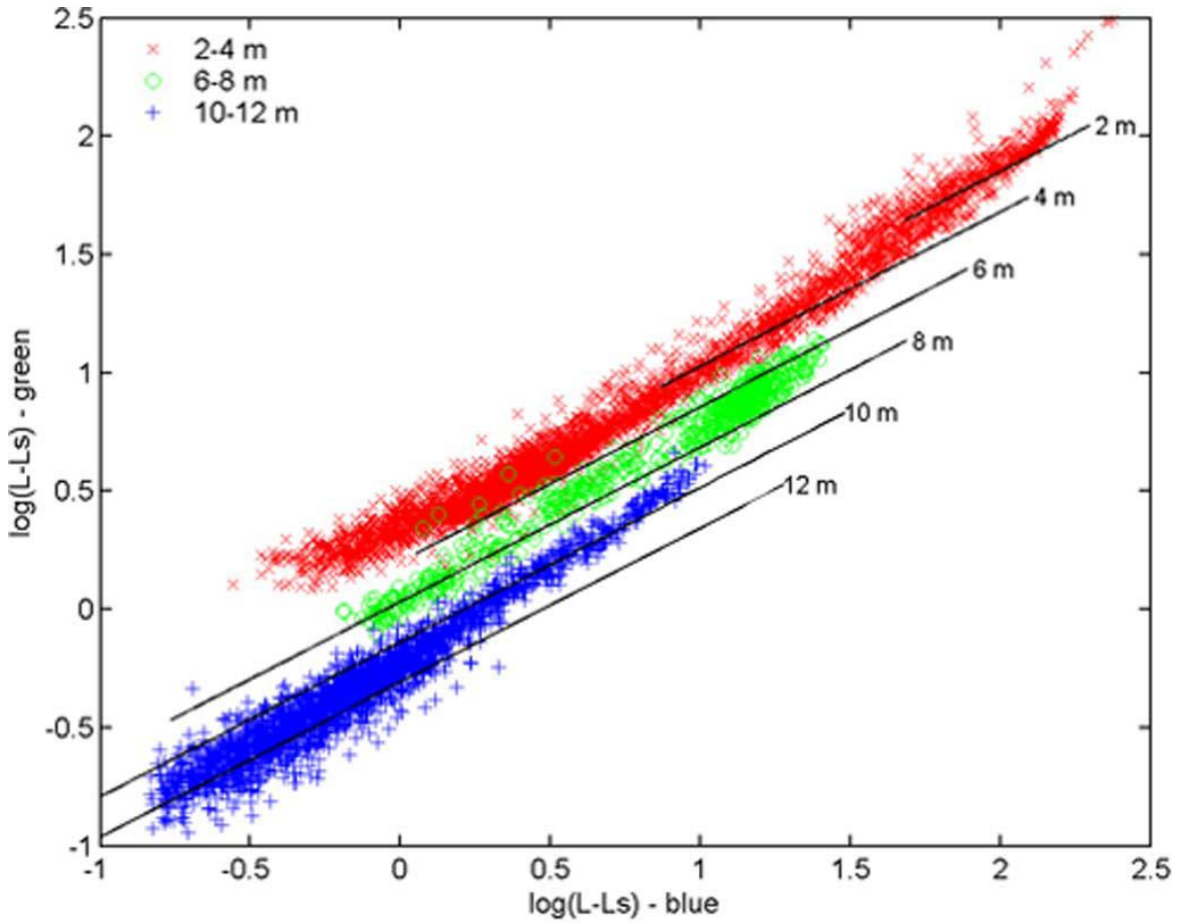

Figure 3. Scatterplot of the logarithmic-transformed blue and green bands at Cancun, Mexico. The red points are between 2–4 m in depth, green between 6–8 m, and blue between 10–12 m. The black lines indicate the predicted graph positions for a specific depth. As the data contain points over different types of bottom cover, some of the variations in point scatter were due to the slightly different reflectance values of the bottom cover rather than the depth itself. Despite the variation, a clear linear relationship can be detected, separated by the depth groups.
Image taken from Lyzenga et al. (2006).

2.3.4. Deriving the optical properties of water

There are two types of optical properties of water: apparent and intrinsic. Apparent optical properties of water (AOPs) are detectable measurements of water that are based on the influence of both light and water, in particularly the angle of light to the water surface (Kirk, 1984). Intrinsic optical properties of water (IOPs) are only based on the water column, such as the scattering coefficient and the light attenuation coefficient (Kirk, 1984). To illustrate, regardless of the properties of the light, the proportion of light scattered or absorbed by a water column will remain the same, as such they are only dependent on the water and its contents.

The HOPE model is based off IOPs, namely the total absorption and total backscatter coefficients. Unfortunately, IOPs are not easily measured owing to the influence of light in real world conditions confounding the measurements of the water column (Gege, 2014; Lee et al., 1998a). As such, these IOPs usually need to be derived.

Common methods to derive IOPs include using an empirical model or approximation equation (Lee et al., 1998b; Ligi et al., 2017), look up table (Wei et al., 2019), machine learning methods (Brockmann et al., 2016), or empirical constants that were calculated based on *ex-situ* measurements of the water column (Bricaud et al., 1981; Morel, 1974). The first two methods involve using empirical data to validate a set of equation(s), before applying the generalised model or equation to other study areas by assuming direct transferability (Lee et al., 1998b; Ligi et al., 2017). The look up table and the machine learning methods relies on using a very large amount of data to set up a reference system or a model to identify the IOPs (Brockmann et al., 2016). While they have more transferability owing to their dataset providing many more environmental conditions than a more basic empirical model, the need for a very large dataset limits this approach. Meanwhile, the most commonly used *ex-situ* measured IOPs are the absorption and the backscatter of the water particles in the water column (Morel, 1974). Although it is the simplest and easiest method as additive properties of IOP coefficients allow each IOP to be easily summed up (Mobley et al., 2004), not all IOPs can be constants as some are dependent on the water quality of each study area (Lee et al., 1998a). As such, the best pilot approach would be to use a mix of known IOP constants and approximation equations. Furthermore, while it is generally difficult to distinguish between the absorption coefficient of gelbstoff and phytoplankton, Lee et al. (1998b) provided an approximation formula for the total absorption coefficient, thereby bypassing the issue of needing to derive each component separately.

2.4. The power and limitations of cloud computing

As a data cube on a cloud platform, GEE provides great parallel computing resources to perform large scale geospatial and temporal analyses in almost an instant without cost. It involves two systems – a server-side system that is the online cluster of computers in the GEE cloud server and the client-side system which is the local computer (Gorelick et al., 2017). While the scripting and commands are done and sent from the local computer, the bulk of the heavy computing is outsourced to the cloud server and the results returned to the local

computer. This offsets most of the computational strain from the local computer to the cloud server, allowing one to easily run complex and large-scaled analysis with only simple computer and an internet access (Mutanga & Kumar, 2019). Furthermore, when saving output into either the online asset or the Google Drive for downloading, once a task has been successfully sent to the cloud server, the GEE cloud server will take over to process the task fully. The local computer is free to execute other programmes or scripts without competing for computer resources for any of the processing, and can even be disconnected from the internet or powered off.

Naturally, there are imposed limitations on the user to avoid user exploits or abuses that may overload the system and in turn deny the service to other users (Gorelick et al., 2017). This GEE usage quota is a major factor that recurs constantly in many different practical restrictions, such as the need for an image composite, the adaptation from an optimisation model to a forward model and a limit on the number of training data for classification. Much of the scripting design is a balance of achieving the scientific aims and circumventing this imposed user limit.

Certain processing methods such as cloud masking consume many resources and would thus exceed the GEE limits when upscaled to large datasets. For example, there are more than 4000 valid images for the coastal seascape of Mozambique. A user request to atmospherically correct all 4000 images would be very resource-intensive and exceed the imposed usage quota. To resolve this, the image is aggregated by composition. The result is an artificial image that does not have much valid or coherent metadata such as the satellite look angles and which pixels are not truly related to its spatially neighbouring pixels and spectral counterparts. Nevertheless, owing to a statistical approach for image composition, the resultant image is still generally representative and can be further processed geospatially.

As part of its approach to be efficient, GEE is designed to be based on vectorisation and thus does not work on a pixel-based approach (Gorelick et al., 2017). However, inversion is a pixel-based approach method rather than a uniform image-based calculation (Klonowski, 2007). Furthermore, the intense computational power required by inversion easily exceeds the imposed GEE usage quota (pers. obs). In order to adapt the semi-analytical model for GEE, it was revamped as a forward model. This necessitated the use of alternatives to derive other variables, namely the SDB and the IOPs, which have been covered in the previous sections.

Similar to the software R, GEE manages a polygonal training data input by converting them into points and then using each point as an independent input (pers. obs.). As such, there will be spatial autocorrelation between points of the same polygon. Furthermore, it inflates the amount of input data and may cause the user to reach the usage quota quicker. This means that the training polygons drawn should be small as well as contain a similar number of pixels within each polygon for all classes. Therefore, the easiest option to manage the vector data for training and validation is to use points instead of polygons.

3. Methodology

3.1. Study region

Mozambique is located in East Africa, about the longitudes of 35° East and 20° South (Figure 4). It has a coastline of about 2500 km which consists of mangroves, seagrasses and coral reefs (Green et al., 2003). Tidal patterns along the shores of Mozambique are not consistent, with the central region having twice the tidal range as compared to other regions (Sete et al., 2002). The seagrasses of Mozambique belong to the Indo-Pacific biosphere. At least fourteen species of seagrasses are known here, including the recently discovered *Thalassodendron leptocaule* (Bandeira et al., 2014; Bandeira & Björk, 2001; Green et al., 2003). While the whole Mozambican seascape is the study area, three focus sites, namely Quirimbas National Park (QNP), Beira and Maputo, will be used to illustrate the analyses in this report. These three sites are also representative of the three different coastal regions described by Green et al. (2003).

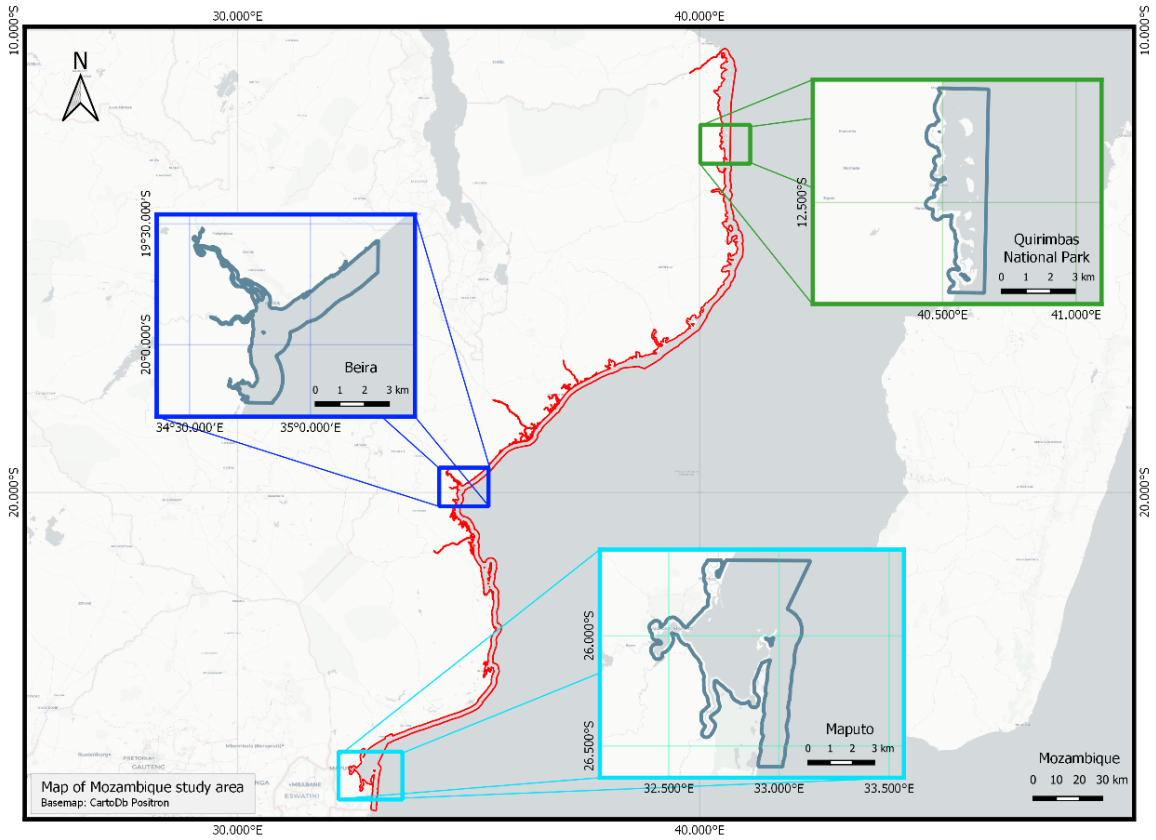

Figure 4. Map of the Mozambican seascape area, demarcated in red. Three subsites were selected to represent the three different types of coast – the rocky limestone coast of Quirimbas National Park, the estuarine coast of Beira and the sandy coast of Maputo.

Although the East African seagrass research has been historically a knowledge gap, some seagrass research has been conducted in Mozambique, such as Maputo (Bandeira et al., 2014; Green et al., 2003). Mozambique is thus a natural choice to develop and validate a seagrass mapping algorithm specific to this region.

Quirimbas National Park is located in the Quirimba Archipelago, which is dominated by rocky limestone (Green et al., 2003). Ten species of seagrasses can be found in this region, including the larger *Enhalus acoroides* and *Thalassodendron ciliatum* (Green et al., 2003). This region is highly dependent on seagrass fisheries for sustenance and survival (Green et al., 2003). Based on tidal station records from a grey literature, the tidal range at Pemba Port, QNP, is 0.25–4.4 m and the mean sea level is 2.25 m (Sete et al., 2002).

Beira is located in the estuarine region, which was not observed to be abundant in seagrass (Green et al., 2003). During the study, it was noted that the waters at and around Beira were highly turbid. It is further assumed that these turbid waters would suppress the growth of seagrasses by limiting the available sunlight in the water (Purvaja et al., 2018). Thus, this is a good site to examine for possible false commissioning. The tidal range is 0.6–7.3 m and mean sea level is 3.56 m (Sete et al., 2002).

Substantial seagrass research has been done in the Maputo Bay, thus providing good ground information about the seagrass there (Bandeira et al., 2014). Nine species of seagrasses are present here, most of which are small-leaved. The bulk of the meadows is located near the Inhaca and Portuguese Islands. While not as turbid as Beira, some turbidity is present due to the large volume of river runoff from the Maputo and Incomati rivers (Markull et al., 2014). Consequently, there is no consistent mean sea level at Maputo, as much of the water level is determined by the precipitation and runoff from the rivers (Sete et al., 2002). The tidal range at Maputo is 1–4 m (Canhanga & Dias, 2005; Sete et al., 2002). There is much sedimentation at Maputo, leading to the formation of several barrier islands (Cooper & Pilkey, 2002).

3.2. Model Approach

The method in this study can be generally categorised into three major components – general geospatial processing, aquatic-specific geospatial processing and classification (Figure 5).

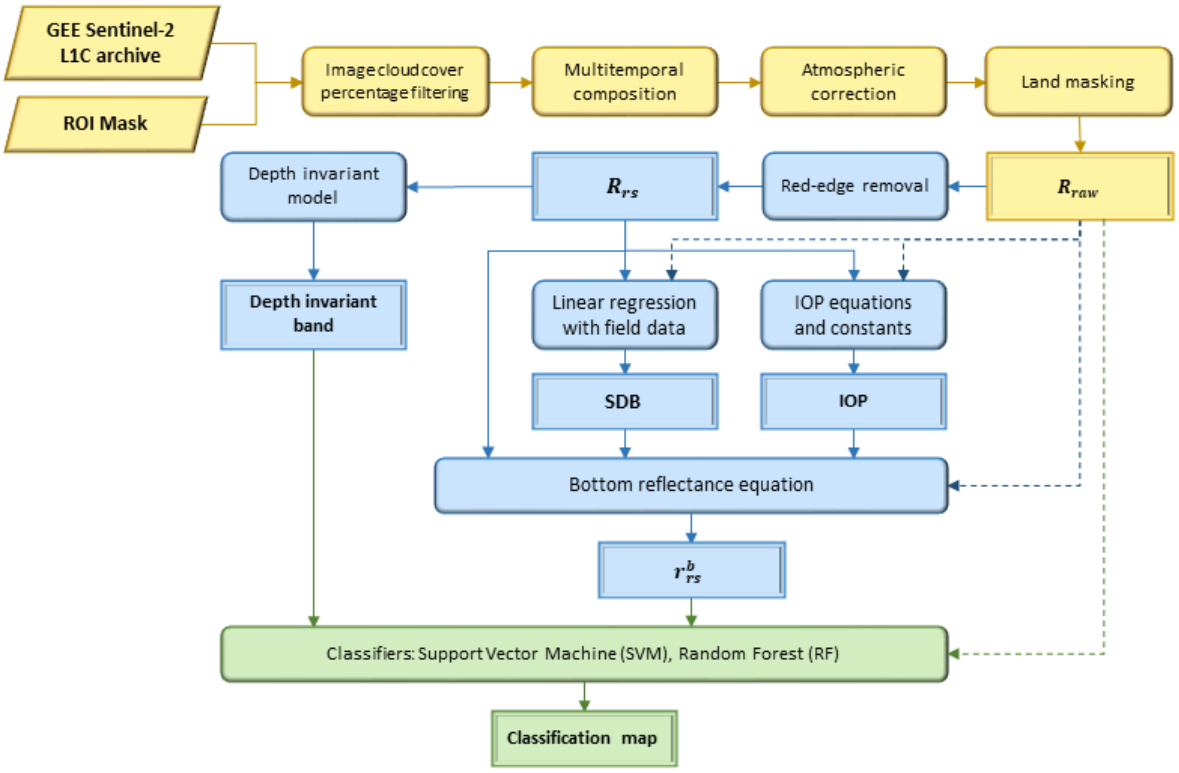

Figure 5. Method overview workflow. Yellow boxes represent processes and products that are not specific to aquatic remote sensing, while blue boxes highlight processes and products of aquatic remote sensing. Green boxes denote classification. The dotted lines from R_{raw} indicates the alternative processing steps done in this study for comparison purposes.

3.2.1. Cloud filtering and Atmospheric correction

More than four years' worth of images in the GEE Sentinel-2 Level-1C Image Collection from 1 June 2015 to 30 November 2019 were used. The Sentinel-2 Level-1C Image Collection was filtered for only images with a cloud cover of less than 2%. The remaining images were then cloud masked using the cloud and cirrus information in the 60 m resolution quality assessment band and subsequently clipped using a region of interest polygon based on a six-nautical-mile distance from the Mozambican coastline, created from the Mozambique Coastline, Internal Waters and Economic Zone shapefiles (Flanders Marine Institute, 2019). Since processing the whole image collection would exceed the GEE-imposed limitation, it was reduced to a single multitemporal composite based on the 20th percentile per pixel, which

reduces the possibilities of selecting a pixel affected by either sun glint, clouds, cloud shadows and other effects (Hird et al., 2017).

3.2.2. Land Masking

After the composition, land pixels were dynamically identified and masked using an Otsu-derived Normalised Difference Water Index (NDWI) threshold based on a 10 m buffered, Canny Edge detection-derived water edge. The composite image was then atmospherically corrected using a Dark Object Subtraction (DOS) based on the SWIR band (Traganos & Reinartz, 2018). The resulting image is the normalised reflectance above the water surface R_{rhown} (Lee et al., 1998a).

3.2.3. Water column correction

In order to account for the difference in optical path between air and water column, the image was further corrected (Traganos & Reinartz, 2018). R_{rhown} was divided by π in order to obtain the remote sensing reflectance just above the water surface, R_{raw}. While R_{raw} is conventionally processed into R_{rs} using a red-edge removal that is based on the black pixel assumption (Siegel et al., 2000), the results of subsequent processes suggest that the red-edge removal did not improve the downstream results. As such, both R_{raw} and R_{rs} were then used to obtain a SDB, the IOPs, the bottom reflectance r_{rs}^{b} , and the DII.

3.2.4. Derivation of Satellite-derived Bathymetry (SDB)

In-situ bathymetry data were collected by the World Wide Fund for Nature (WWF) and local citizens using a boat-based sonar. Owing to limited resources, bathymetry data were only collected from the waters at QNP, Angoche and Moma. As there are multiple data points within a Sentinel-2 pixel-equivalent area of 10 m × 10 m, a mean depth per pixel area was calculated. Thus, a total of 1747 field points were used. By iterating the regression 30 times using randomised data partitions ranging between 0.1 and 0.9, the best data partition ratio of 9:1 was obtained and subsequently used, resulting in 1573 training points and 172 validation points. A multi-linear regression was performed on the first four bands of R_{rs} to derive the slopes b and intercepts x of each band (i, j, k, l) for the estimation of the SDB in Equation (1) (Lyzenga, 1985).

$$z = a + b_i x_i + b_j x_j + b_k x_k + b_l x_l \quad (1)$$

A systematic underestimation of depth was also assumed, as the resultant SDB had negative depth estimates that were more than the maximum tidal height of the region (approximately -4.5 m in depth). As such, a systematic shift was performed to shift all values into the positive domain by subtracting all values with the minimum.

3.2.5. Derivation of Intrinsic Optical Properties of water (IOPs)

In order to obtain r_{rs}^{b} , the absorption and backscatter coefficients of water at 440 nm have to be derived from R_{rs} (Lee et al., 1998a). Table 1 summarises the various methods and models used to obtain these IOPs. The total absorption coefficient, a_{tot}, was obtained using an approximation formula as stated in Equation (3) (Lee, 1994). The a_{tot} values were constrained between 0 and 150 in order to handle the rare cases of extreme values from approximation (Dierssen et al., 2019). Meanwhile, the backscatter coefficient of water was obtained from Bricaud et al. (1995) and of suspended particles based on Lee's equations (Lee et al., 1998b).

$$\rho_{ij} = log_{10}\left[\frac{R_{rs}(\lambda_i)}{R_{rs}(\lambda_j)}\right] \quad (2)$$

$$a_{tot}(440) = 10^{-0.674 - 0.531\rho_{25} - 0.745\rho_{25}^2 - 1.469\rho_{35} + 2.375\rho_{35}^2} \quad (3)$$

Separately, the IOP values were validated by comparing against the output of the Case-2 Regional / Coast Colour (C2RCC) processor based on a single Sentinel-2B Level-1C image from Mozambique on 27 June 2019, derived from R_{rs}. The scene was atmospherically corrected using the Aquatic Atmospheric Correction in Sen2Cor version 2.80, producing R_{rhown} as well as a_{tot} at 443 nm. The resultant R_{rhown} was then processed with this study's method to produce the approximated a_{tot} at 440 nm. Although the C2RCC product was based on

Table 1. Table detailing the methods used to derive the coefficients of these five intrinsic optical properties of water used in the HOPE model.

IOP	Model	Reference
Absorption		
Total (water, phytoplankton and gelbstoff)	Analytical (approximation)	Lee et al. (1998b)
Backscatter		
Water	Constant	Morel (1974)
Suspended particles	Analytical	Gordon & Morel (1983)

MERIS's 443 nm output (Brockmann et al., 2016), the differences were very minor when the IOP values were converted from the current 440 nm output to the predicted 443 nm output using Equation (4) (Austin & Petzold, 1986). Thus, a direct comparison was done without converting the approximated a_{tot} to the same wavelength.

$$K(\lambda_2) = \frac{M(\lambda_2)}{M(\lambda_1)} [K(\lambda_1) - K_w(\lambda_1)] + K_w(\lambda_2) \quad (4)$$

where Krepresents the attenuation coefficient of interest a_{tot} , λ_1 and λ_2 are the source and the desired wavelengths respectively, and $M(\lambda_x)$ and $K_w(\lambda_x)$ are the slope function and attenuation coefficient of water respectively based on Austin & Petzgold (1986).

3.2.6. Derivation of the bottom reflectance

The derived SDB and IOP were then used in conjunction with R_{rs} as input into Lee's model (Lee et al., 1998a) to derive r_{rs}^b. Using Lee's shallow water approximation based on the Hydrolight simulations (Lee, Carder, Mobley, Steward, & Patch, 1999), the below water surface reflectance r_{rs} is derived from R_{rs}. The derived SDB and IOP will then be used together with r_{rs} as input for Lee's equation (Lee et al., 1998a) in Equation (5) to obtain r_{rs}^b, which is represented by ρ in the equation.

$$\begin{aligned} r_{rs} &= r_{rs}^c + r_{rs}^b \\ &\approx r_{rs}^{dp} \left\{1 + \exp\left[-\left(\frac{1}{\cos(\theta_w)} + \frac{D_u^c}{\cos(\theta_v)}\right) \kappa H\right]\right\} \\ &\quad + \frac{1}{\pi} \rho \left\{1 + \exp\left[-\left(\frac{1}{\cos(\theta_w)} + \frac{D_u^b}{\cos(\theta_v)}\right) \kappa H\right]\right\} \end{aligned} \quad (5)$$

where r_{rs}^{dp} is the sub-surface remote sensing reflectance and the various other parameters are:

$$r_{rs}^{dp} \approx (0.084 + 0.170u)u \quad (6)$$

$$D_u^c \approx 1.03(1 + 2.4u)^{0.5} \text{ and } D_u^b \approx 1.04(1 + 5.4u)^{0.5} \quad (7)$$

$$u = \frac{sum\ of\ backscatter\ coefficients}{sum\ of\ absorption\ and\ backscatter\ coefficients} \quad (8)$$

As the current image is a temporal composite, there is no metadata for the solar zenith angle, θ_w, and the satellite viewing angle, θ_v. Based on the assumption that the final composite image is equivalent to an image taken at nadir, θ_v was set to 1 (Traganos & Reinartz, 2018).

By calculating the mean θ_w of all relevant images used in the GEE Sentinel-2 Image Collection, a θ_w value of 38.65° was used. Equation (5) can be rearranged as a ρ-centric in Equation (9).

$$\rho = \pi \frac{r_{rs} + r_{rs}^{dp}\left[e^{-\kappa H\left(\frac{1}{\cos\theta_w} + D_u^c\right)} - 1\right]}{e^{-\kappa H\left(\frac{1}{\cos\theta_w} + D_u^c\right)}} \quad (9)$$

The denominator $e^{-\kappa H\left(\frac{1}{\cos\theta_w} + D_u^c\right)}$ in Equation (9) may occasionally produce a very small value close to zero, which in turn greatly inflates ρ. As such, a constraint of 0.001 to 10 was applied to the calculated denominator (Dierssen et al., 2019). It was observed that r_{rs}^b would have a more reasonable range of values when ρ was transformed by a division of 100. As such, the scaling was performed and both original and scaled r_{rs}^b were used for classification.

3.2.7. Derivation of additional features using the Depth Invariant Index (DII)

The DII is a relative depth feature based on R_{rs}. For the same bottom cover, a logarithm-transformed plot of the atmospherically corrected radiance for band i and the similarly transformed band j is linearly related with a constant gradient. The gradient of the linear regression is the ratio of the attenuation coefficient, $\frac{k_i}{k_j}$, which is only affected by the wavelength of the selected bands and water clarity. Thus, the linear equation can be rearranged to create the DII in Equation (10). Unlike the SDB, the DII is not affected by the brightness or darkness of the pixel reflectance within the same bottom cover class. Between different bottom cover classes, while the gradient for the regression line remains the same, the resulting DII values are parallel shifts. Therefore, the DII would provide some distinction between classes of similarly bright or dark pixels.

$$Depth\ invariant\ index_{ij} = ln(L_i - L_{si}) - \left[\left(\frac{k_i}{k_j}\right).ln(L_j - L_{sj})\right] \quad (10)$$

where, for bands i and j, the various other parameters are:

$$\frac{k_i}{k_j} = a + \sqrt{(a^2 + 1)} \quad (11)$$

$$a = \frac{\sigma_{ii} - \sigma_{jj}}{2\sigma_{ij}} \quad (12)$$

where σ_{ii} is the covariance of band i, σ_{jj} is the covariance of band j, and σ_{ij} is the covariance between bands i and j.

3.3. Classification

3.3.1. Raster data

As there were modifications to the standard semi-analytical model when adapting to the GEE platform, one R_{raw} and four differently processed r_{rs}^{b} products were classified. R_{raw} was an input image, as it is conceptually similar to a terrestrial atmospherically corrected image. R_{rs}, however, was not used as input image as the standard procedure is to use R_{rs} to derive other layers. In order to investigate the impact of the red-edge correction between R_{raw} and R_{rs}, the r_{rs}^{b} products of both images were classified. Finally, the influence of rescaling the r_{rs}^{b} products was explored through a comparison of classification output between the original and scaled r_{rs}^{b} products of both the R_{raw} and R_{rs}.

3.3.2. Training and Validation data

Training data were created in GEE using the R_{rs} image as well as the GEE satellite image base map. As GEE processes polygons by converting them into spatial points for every pixel in the polygon, not only would more care be needed to create similarly-sized training polygons, there would also be a strong spatial autocorrelation between pixels of the same polygon. Thus, training points were used instead. A total of 765 training points was used for the 8 selected subclasses (Table 2). Based on a 7:3 ratio, the points were then partitioned into the training and validation dataset.

Table 2. Table showing the classes and subclasses of the training data.

Class	Subclass
Optically deep water	Deep water
Turbid water	Turbid water
Bright substrate	Bright substrate in clear water
Bright substrate	Bright substrate in turbid water
Dull substrate	Dull substrate in clear water
Dull substrate	Dull substrate in turbid water
Seagrass	Seagrass in clear water
Seagrass	Seagrass in turbid water

3.3.3. Classification

Classification was done in the GEE using both Support Vector Machine (SVM) and Random Forest (RF) classifiers. An SVM gamma and cost of 10 was used, as an exploratory

hyperparameter search found that the maximum gamma and cost values should not exceed 100. As for the RF hyperparameter, 10 trees were set.

Post-classification, the subclasses were combined before an accuracy assessment was performed. The predicted seagrass cover in the classification maps were then used to estimate the areal cover of seagrasses in Mozambique.

4. Results

4.1. Satellite-derived Bathymetry (SDB)

The SDB derived from R_{raw} had a better R^2 but worse RMSE than that of R_{rs} (Table 3). Both SDB layers also seemed to underestimate the water depth, given their statistical values. The extreme values R_{raw}-derived SDB seemed to underestimate the depth less than those of R_{rs} -derived SDB. Nonetheless, the median depth estimated by both layers were quantitatively close with a difference of only 1.43 m as compared to the differences between their estimated minimum and maximum depth, which were 7.72 m and 9.23 m respectively.

Table 3. Quantitative comparison between the best SDB products derived from R_{raw} and R_{rs} layers, to 2 decimal places. For both layers, a data partition of 9:1 was used. A dot decimal separator is used in this table.

Statistics	R_{raw}-derived SDB	R_{rs}-derived SDB
R^2	0.68	0.58
RMSE	4.14	2.61
Minimum depth (m)	-10.63	-18.35
Median depth (m)	3.38	4.81
Maximum depth (m)	22.06	12.83

Based on the SDB at QNP and Maputo, the estimation of water depth in non-turbid waters seems to be fit well with features visible in the 3-2-1 false colour composite, especially in the midwaters and deep waters (Figure 6 & Figure 8). However, the depth estimation in shallow waters could still be further improved, as QNP had depth estimates of up to -4.73 m (Figure 6).

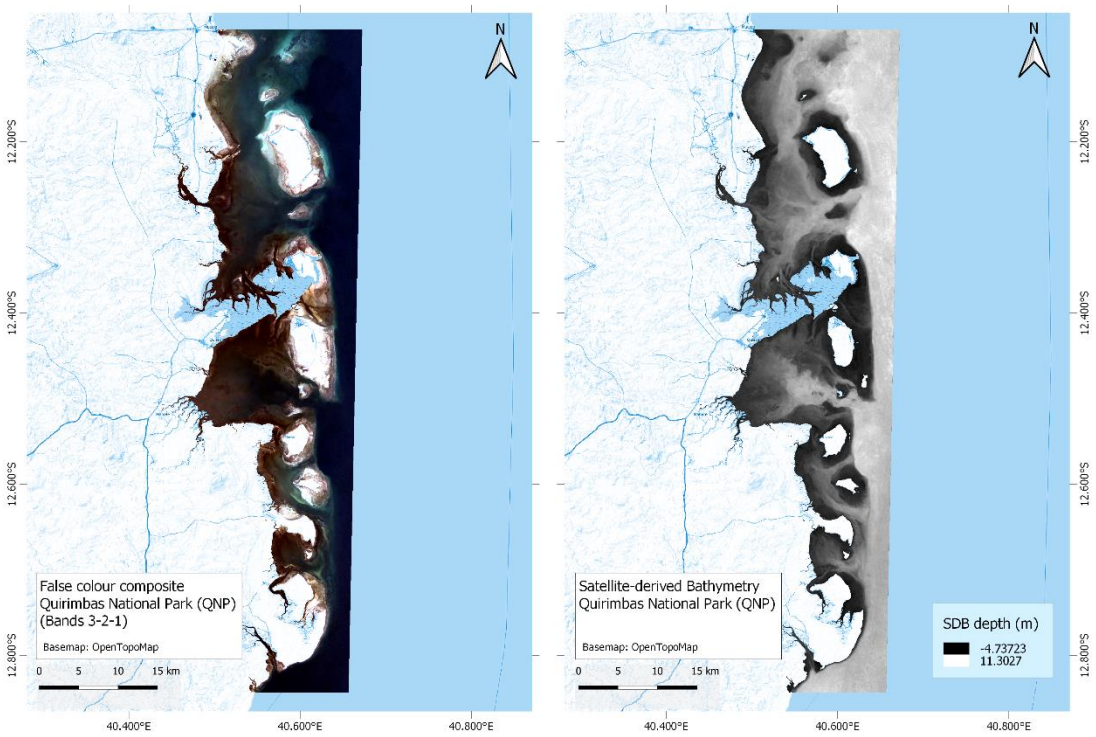

Figure 6. Sentinel-2 bands 3-2-1 false colour composite (left) and R_{raw}-derived Satellite-derived Bathymetry (right) of QNP.

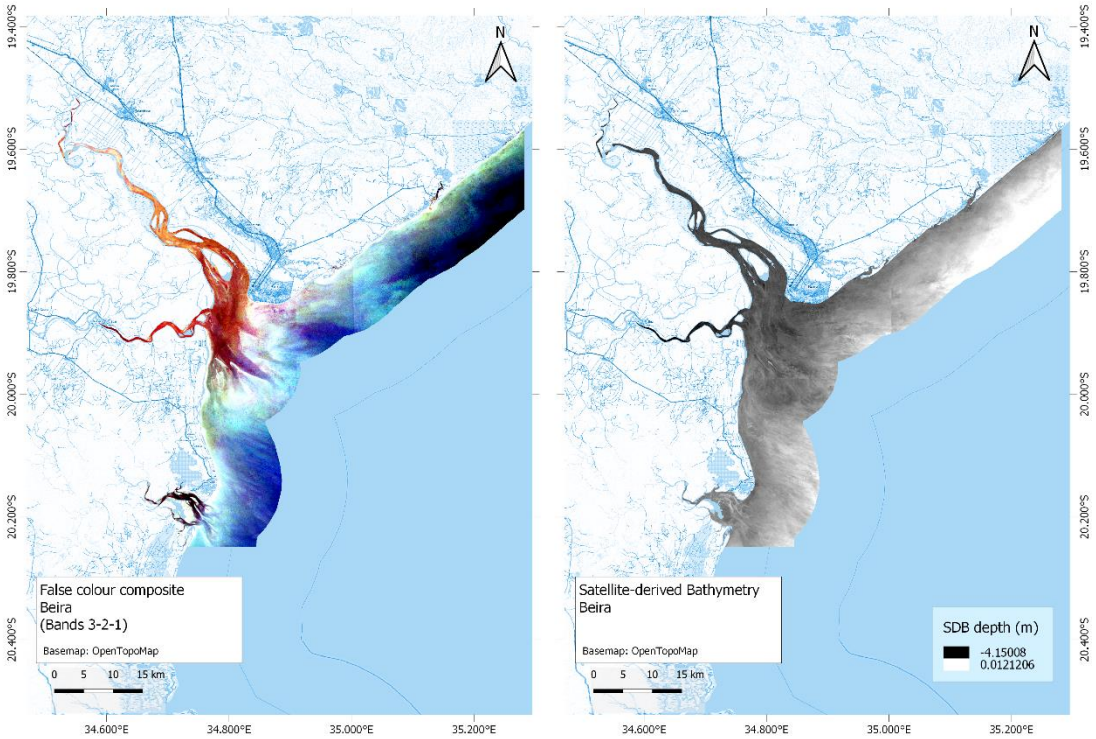

Figure 7. Sentinel-2 bands 3-2-1 false colour composite (left) and R_{raw}-derived Satellite-derived Bathymetry (right) of Beira.

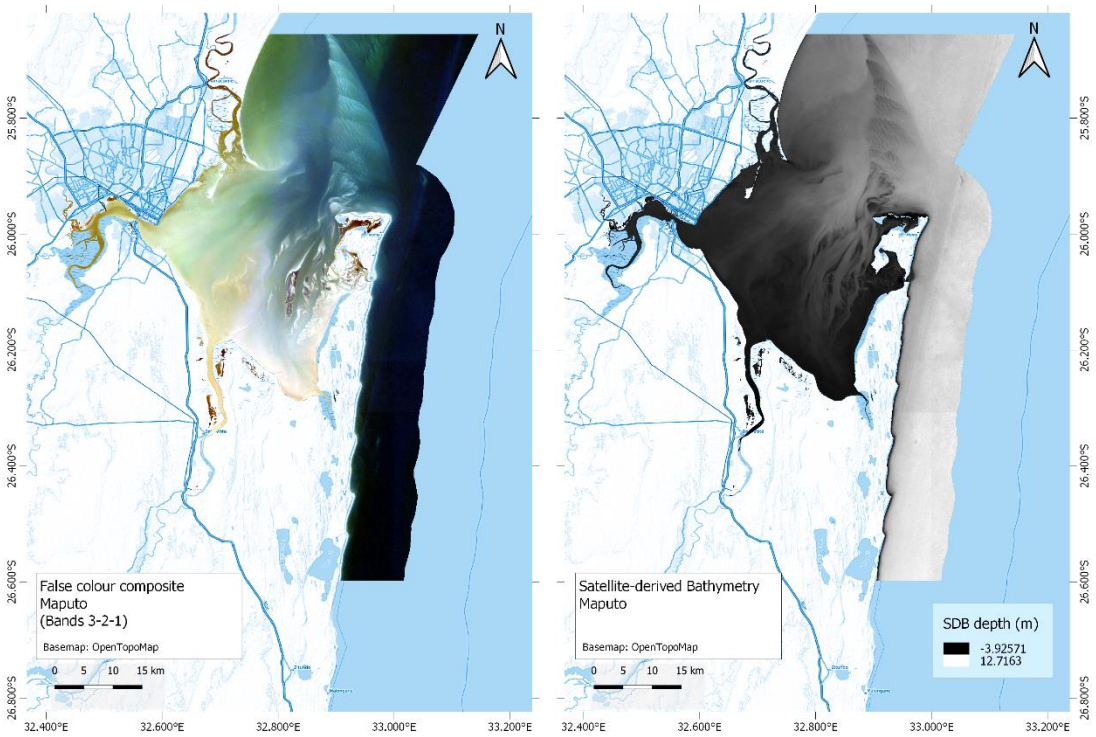

Figure 8. Sentinel-2 bands 3-2-1 false colour composite (left) and R_{raw}-derived Satellite-derived Bathymetry (right) of Maputo.

The SDB estimates performed badly in turbid waters. The linear regression model was unable to distinguish highly turbid waters from shallow waters, such as Beira (Figure 7) and the murkier waters flowing out of the Maputo River mouth (Figure 8). While the minimum depth at Beira had similar shallow water issues with QNP and Maputo, its maximum depth of 0.01 m is wrong as the pixels furthest from the Beira coastline are six nautical miles away and thus definitely mid to deep water pixels (Figure 7).

After the systematic shift, the maximum values of R_{raw} and R_{rs} are comparable (Table 4). However, there is a sizeable difference of 37.00% in median values between both layers. This is the opposite of the pre-shift estimates that were previously mentioned, implying much difference between their SDB estimates.

Table 4. Post-systematic shift quantitative comparison between the best SDB products derived from R_{raw} and R_{rs} layers, to 2 decimal places. R^2 and RMSE are left out as they are assumed to be irrelevant after the shift. A dot decimal separator is used in this table.

Statistics	**R_{raw}-derived SDB**	**R_{rs}-derived SDB**
Minimum depth (m)	0.00	0.00
Median depth (m)	14.00	22.22
Maximum depth (m)	32.69	31.18

4.2. Intrinsic Optical Properties of water

4.2.1. Comparison between C2RCC and approximation algorithm

Based on a single scene comparison, most of the approximated a_{tot} values are within 25% difference from the C2RCC equivalents (Figure 9). Shallow water pixels generally have a smaller difference than deeper water pixels, although differences above 25% and extreme differences above 100% may be found on the edges around the corals reefs as well as the riverine banks of the mangrove (Figure 10). The most frequent difference is 10%, and then 9%, which are more likely to be the general difference from the C2RCC values. There is another peak at 3%, although it is an acute mode that falls off fast. While there were extreme differences of more than 400%, these differences were very rare occurrences.

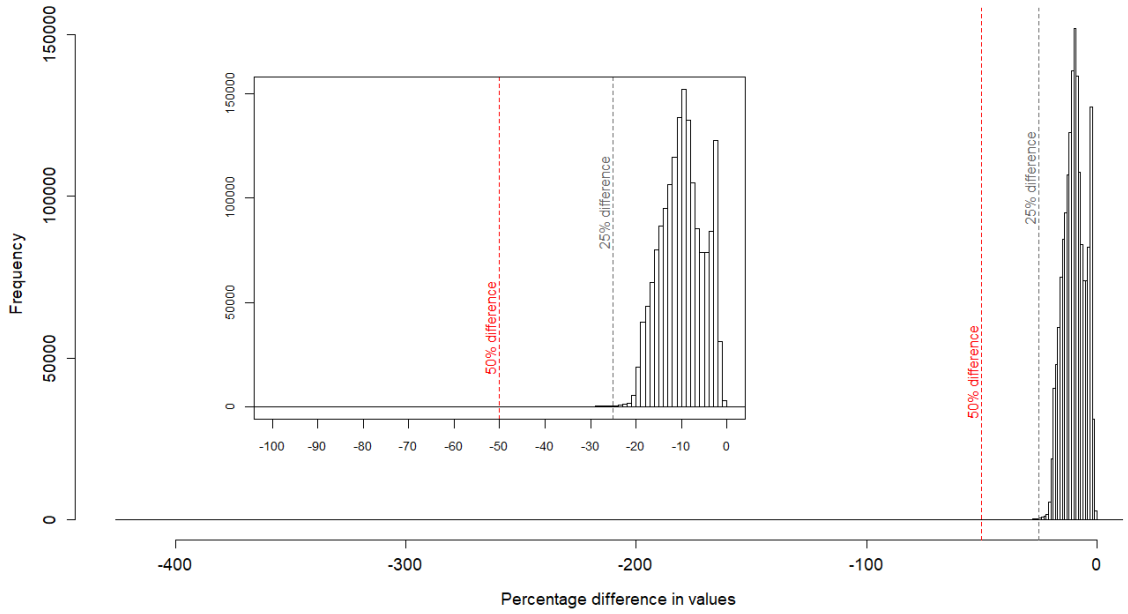

Figure 9. Histogram showing percentage difference in predicted a_{tot} between the C2RCC product and the approximation formula by Lee et al. (1998b), based on a single Sentinel-2 Level-1C image in Mozambique on 27 June 2019. Most of the pixels differ by less than 25%. The largest difference is at 3%, although the peak is very narrow. A broader, second highest peak lies at the 10% difference mark.

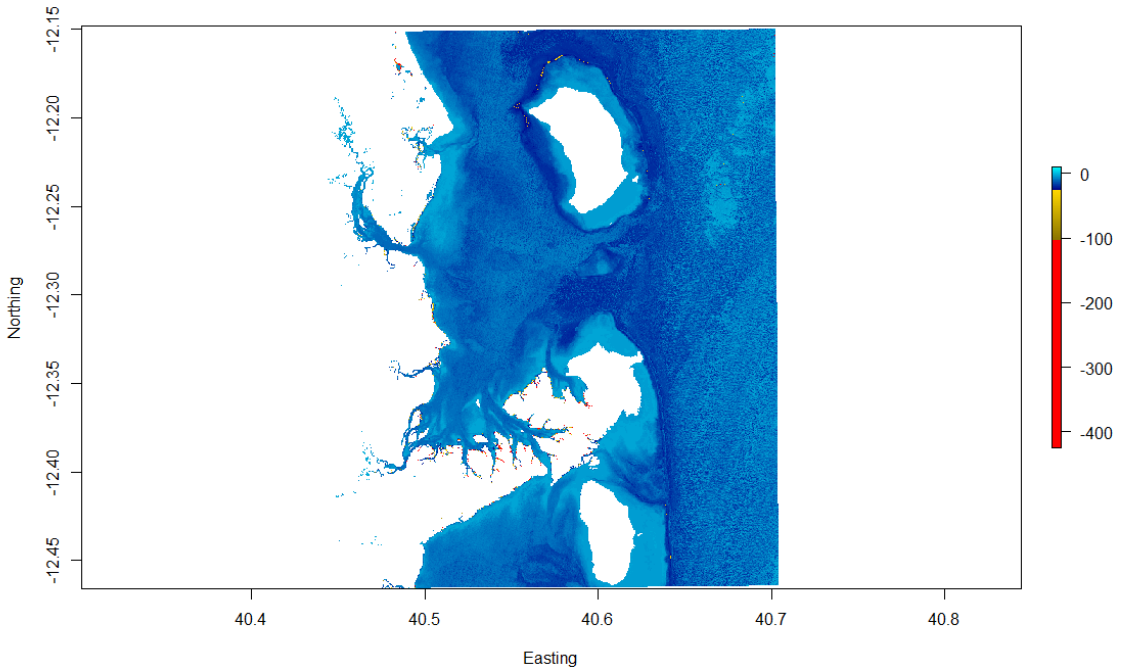

Figure 10. Map showing percentage difference in predicted a_{tot} between the C2RCC product and the approximation formula by Lee et al. (1998b). Pixels from about 0% to 25% are coloured in increasingly darker shade of blue, 25% to about 100% coloured yellow to brown. Beyond a 100% difference, the areas are shaded in a homogeneous red. The projection in this map is the WGS 1984 UTM Zone 37S.

4.2.2. Comparison between the R_{raw} and R_{rs} IOP products

While the a_{tot} products of R_{raw} and R_{rs} seemed to be initially similar based on their similar mean and minimum values, their maximum values differ largely (Figure 11). The greatest difference was the maximum value of the B1 band – the R_{raw}-derived had a maximum value of 147.183 as compared to 1.602 for the R_{rs}-derived product. Given that the mean values remained similar, it can be inferred that the maximum values are rare extremes that are not representative of the approximation equation's performance. In contrast, while the b products of R_{raw} and R_{rs} had similar minimum values and slightly differing maximum values, their mean values were largely different (Figure 12). This infers that the b products are more dissimilar and only share their similar extreme values coincidentally. Also, despite the significantly lesser maximum values, the mean b for R_{rs} is greater than its mean a_{tot}, implying that more pixels in Mozambique had a greater backscatter effect than an absorption effect for the R_{rs} product.

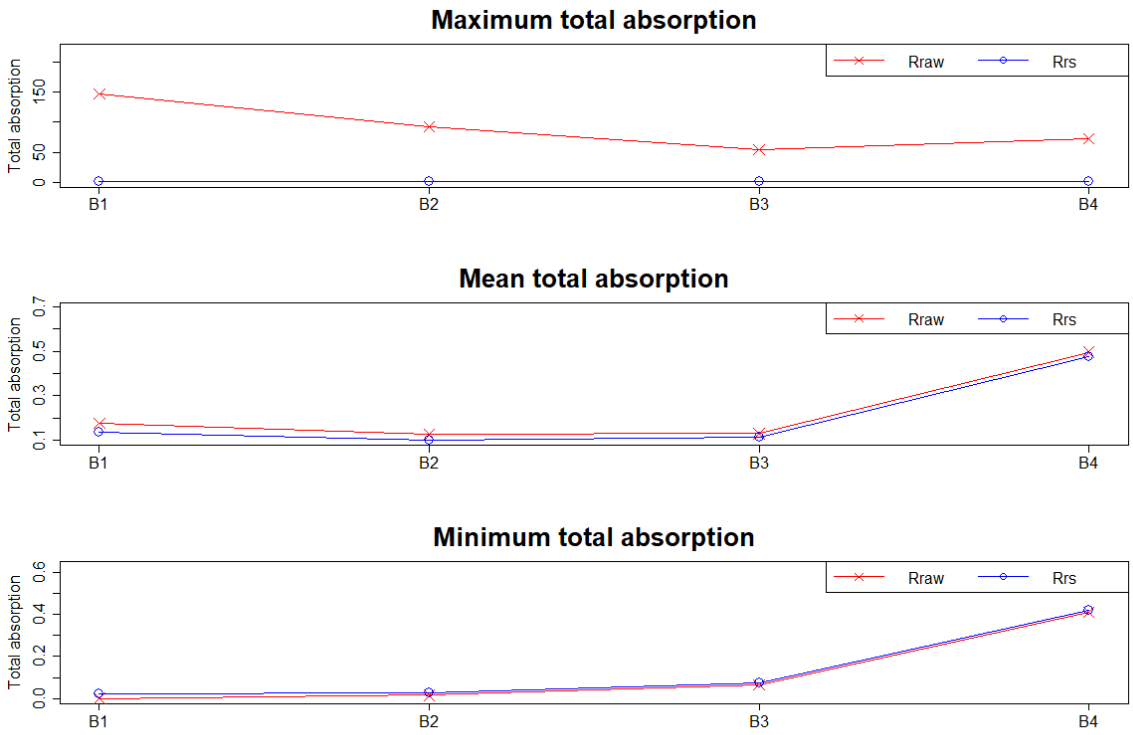

Figure 11. Comparison of maximum, mean and minimum a_{tot} values between the products derived from R_{raw} (red) and R_{rs} (blue).

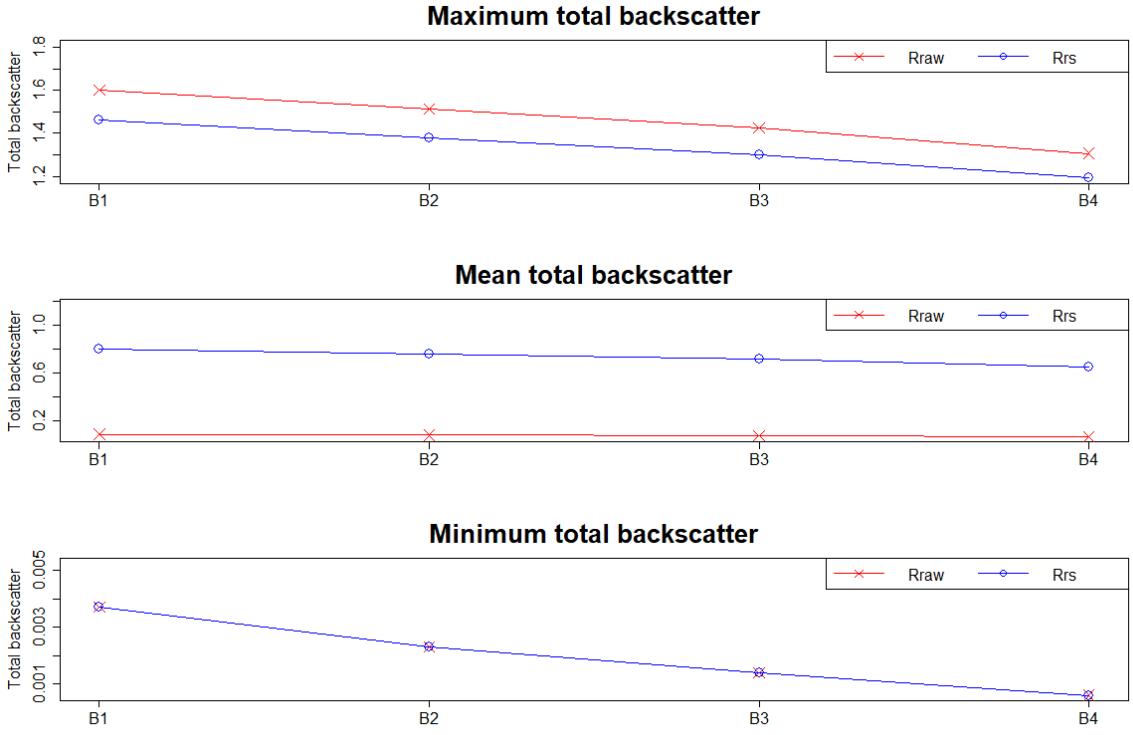

Figure 12. Comparison of maximum, mean and minimum b values between the products derived from R_{raw} (red) and R_{rs} (blue).

4.3. Bottom reflectance

The initial r_{rs}^{b} products had spectral values that were too large in magnitude for a reflectance product (Figure 13). Post-scaling, the spectral values were within standard values for a reflectance product (Figure 14). A visual comparison between Figure 13 and Figure 14 found that the spectral curves are conserved during the scaling. Further comparison between the initial and scaled products also supported the conservation of spectral curve during transformation.

Between the products from R_{raw} and R_{rs}, there are dissimilarities in spectral curves of the same subclasses (Figure 15 & Figure 16). The two bright substrate subclasses are almost separated from other subclasses in all four bands of the R_{raw}-derived product, and only had interquartile overlaps with the dull substrate in turbid water and deep water subclass. However, the seagrass subclasses have a large spectral distribution overlap with the deep water, turbid water and dull substrate in clear water subclasses. Unexpectedly, the deep water subclass had a large variation in values for both its interquartile range and full distribution, even more than the turbid water subclass in the first two bands and B3 band for the interquartile only (Figure 15). Meanwhile, subclasses of the R_{rs}-derived product generally had a narrower interquartile range and distribution, especially the deep water and turbid water subclasses. Unlike their R_{raw}-derived counterparts, the bright substrate subclasses were spectrally dissimilar, except for the B4 band. Instead, the bright substrate in turbid water subclass had more spectral similarities with the dull substrate in clear water subclass. There was also a distinction between the deep water and turbid water subclasses. Conversely, the dull substrate subclasses became more spectrally similar. While the seagrass subclasses were still spectrally similar, they retained their spectral overlap with the turbid water and dull substrate in turbid water subclasses. Although there is a slight separation between the seagrass subclasses and the dull substrate subclass in the B4 band, their interquartile ranges still overlap with the turbid water subclass (Figure 16).

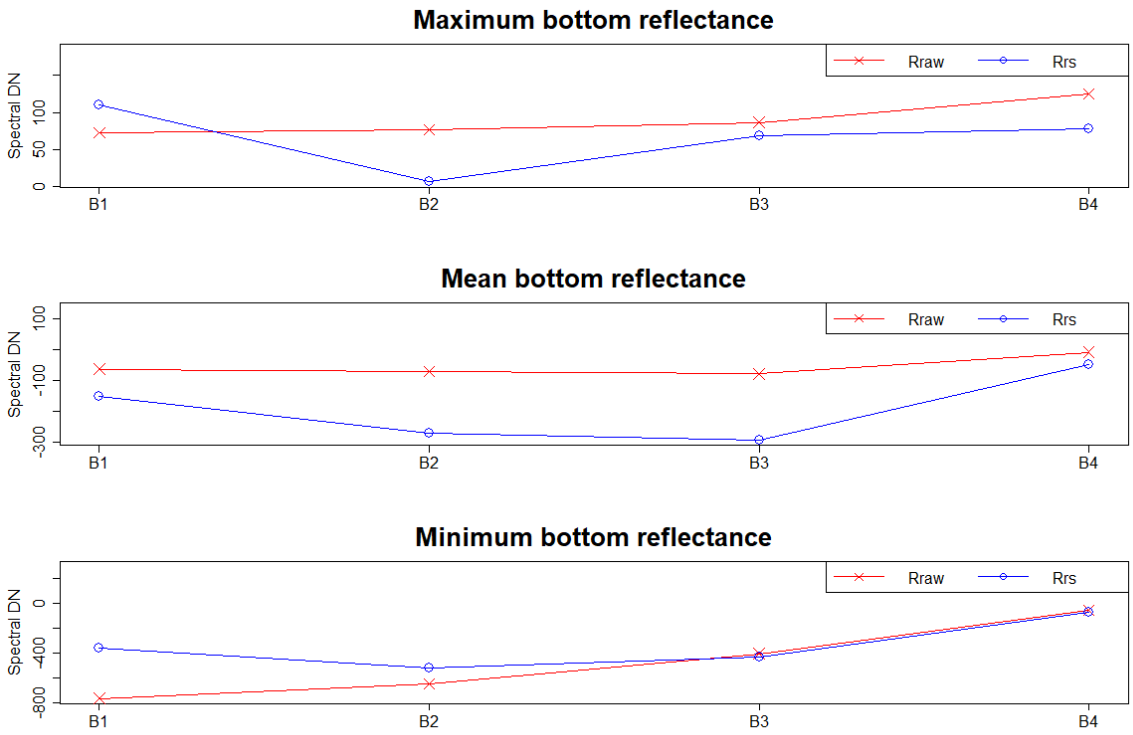

Figure 13. Comparison of maximum, mean and minimum values of the initial r_{rs}^{b} between the products derived from R_{raw} (red) and R_{rs} (blue).

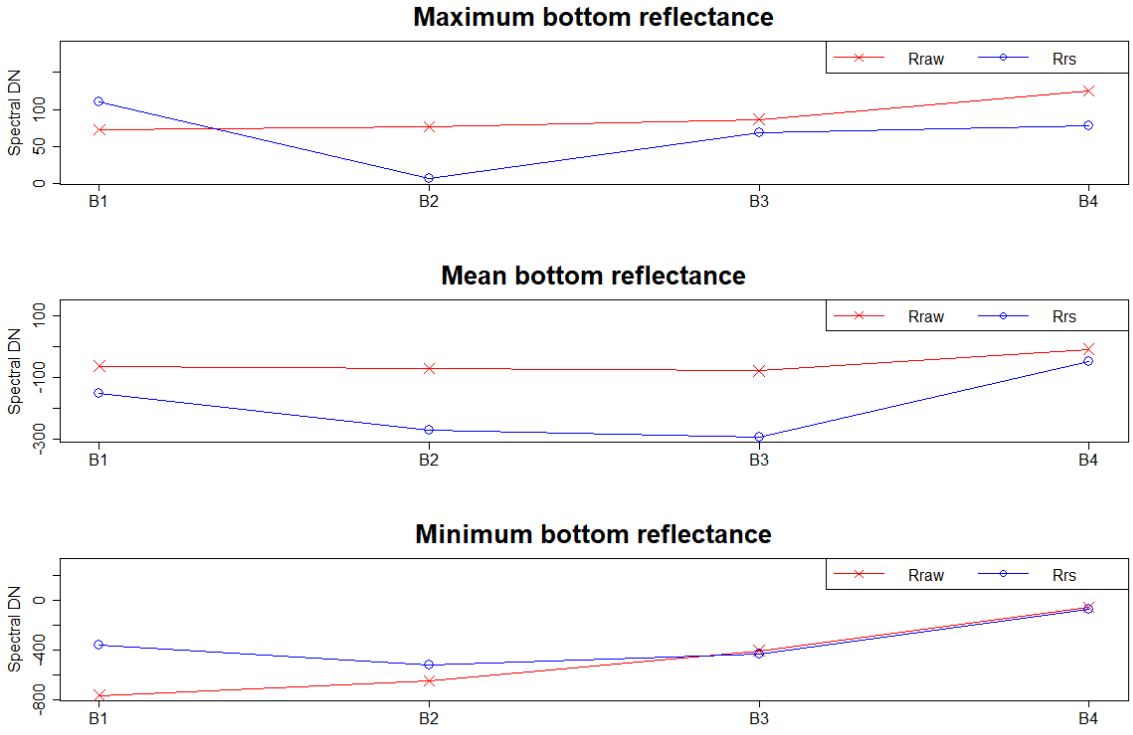

Figure 14. Comparison of maximum, mean and minimum values of the scaled r_{rs}^{b} between the products derived from R_{raw} (red) and R_{rs} (blue).

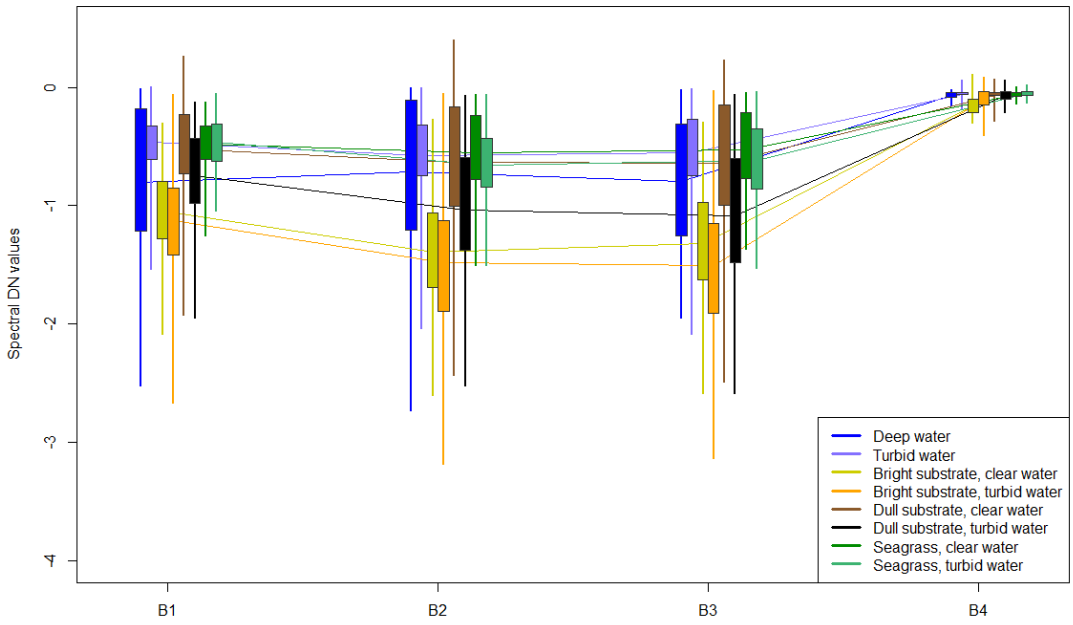

Figure 15. Comparison of subclass spectral curves for the scaled r_{rs}^{b} derived from R_{raw}. These values were extracted using the training vector data. The box plot denotes the 1st and 3rd quantile, while the vertical lines denote the minimum and maximum values of each subclass. The unscaled R_{raw} is not shown as the spectral curve is the same, except the DN values are 100 times larger.

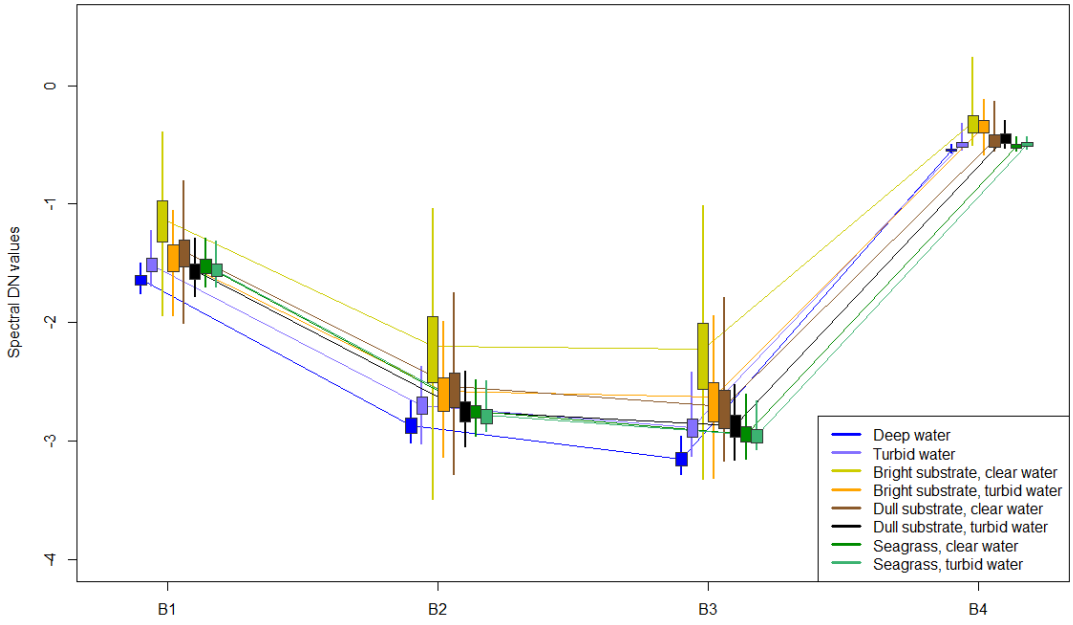

Figure 16. Comparison of subclass spectral curves for the scaled r_{rs}^{b} derived from R_{rs}. These values were extracted using the training vector data. The box plot denotes the 1st and 3rd quantile, while the vertical lines denote the minimum and maximum values of each subclass. The unscaled R_{rs} is not shown as the spectral curve is the same, except the DN values are 100 times larger.

4.4. Classification

Quantitatively, the best SVM classification is based on the scaled R_{rs}-derived r_{rs}^b (Table 5). The SVM classifier is sensitive to the input values and fared badly on the initial r_{rs}^b products. Both r_{rs}^b products produced a classification map with only the turbid water class, which is not descriptive of the Northern (Figure 17) and Southern (Figure 19) coasts of Mozambique. Despite its obvious classification failure, this was ironically the most accurate qualitative description of the turbid Beira site (Figure 18).

While the overall accuracy for all five RF classification maps were similar, the R_{raw} classification map had the worst seagrass producer's accuracy (PA), and the scaled R_{raw}-derived r_{rs}^b and the initial R_{rs}-derived r_{rs}^b classification maps had the best two seagrass PA (Table 6). Between SVM and RF, RF had a more quantitatively consistent performance with seagrass identification (Table 5 & Table 6). Also, RF was not largely affected by the scaling issues of the r_{rs}^b products on the quantitative accuracy. However, the RF classification maps were generally noisier than the SVM classification maps, even after aggregating the subclasses (Figure 17 – Figure 19).

Barring the erroneous single class accuracy matrix of the initial r_{rs}^b SVM maps, the deep water class was the best classified class (Table 5 & Table 6). Although the spectral variations within

Table 5. SVM Classification accuracy between various products derived from R_{raw} and R_{rs} layers. A total of five final classes were used – seagrass, deep waters, bright substrate, dull substrate and turbid waters. PA denotes producer's accuracy and UA denotes user's accuracy.

Statistics (%)	R_{raw}	r_{rs}^b , R_{raw}-derived		r_{rs}^b , R_{rs}-derived	
		Initial	Scaled	Initial	Scaled
Seagrass PA	22.45	0.00	42.86	0.00	51.02
Seagrass UA	34.38	0.00 [a]	39.62	0.00 [a]	65.79
Deep water PA	86.67	0.00	93.33	0.00	90.00
Deep water UA	68.42	0.00 [a]	80.00	0.00 [a]	81.82
Bright substrate PA	54.00	0.00	54.00	0.00	70.00
Bright substrate UA	75.00	0.00 [a]	71.05	0.00 [a]	71.43
Dull substrate PA	30.30	0.00	33.33	0.00	42.42
Dull substrate UA	33.90	0.00 [a]	50.00	0.00 [a]	54.90
Turbid water PA	68.97	100.00	48.28	100.00	68.97
Turbid water UA	33.90	12.95	25.93	12.95	37.74
Overall accuracy	46.43	12.95	50.00	12.95	60.27

[a] No pixels were assigned as seagrass.

Table 6. RF Classification accuracy between various products derived from R_{raw} and R_{rs} layers. A total of five final classes were used – seagrass, deep waters, bright substrate, dull substrate and turbid waters. PA denotes producer's accuracy and UA denotes user's accuracy.

Statistics (%)	R_{raw}	r_{rs}^{b} , R_{raw}-derived		r_{rs}^{b} , R_{rs}-derived	
		Initial	Scaled	Initial	Scaled
Seagrass PA	34.69	40.82	53.06	48.98	40.82
Seagrass UA	47.22	45.45	50.00	55.81	50.00
Deep water PA	86.67	86.67	90.00	83.33	83.33
Deep water UA	78.79	81.25	79.41	78.13	86.21
Bright substrate PA	80.00	66.00	66.00	74.00	76.00
Bright substrate UA	75.47	68.75	71.74	75.51	79.17
Dull substrate PA	48.48	37.88	31.82	45.45	51.52
Dull substrate UA	60.38	53.19	50.00	60.00	54.84
Turbid water PA	48.27	62.07	58.62	58.62	65.52
Turbid water UA	28.57	33.96	34.00	34.00	42.22
Overall accuracy	57.59	54.46	55.36	59.38	60.71

this class were greater in the R_{raw}-based products (Figure 15), its producer's accuracy were better. Besides the deep water class and the seagrass class for the RF classifier, the producer's accuracy generally improved when using the R_{rs}-derived products instead. Also, owing to the similar spectral curves of their subclasses (Figure 15 & Figure 16), the turbid water, dull substrate and seagrass classes were easily misidentified by the classifiers as the other two classes. This was most telling at the Beira site, where much of the turbid water pixels were classified as either of these classes. Despite the greater spectral difference between the bright substrate and the turbid water class in R_{rs} (Figure 16), many turbid water pixels at the mouth of the Beira River were classified instead as bright substrate in the scaled R_{rs}-derived r_{rs}^{b} maps (Figure 18). As the same area was also misidentified by the SDB as above sea level (Figure 7), this bright substrate classification might also be the input of depth information through either the SDB or the DII. Based on the overview maps of the three sites, the R_{raw}-derived products were noisier than the R_{rs}-derived products of the same classifier (Figure 17 – Figure 19).

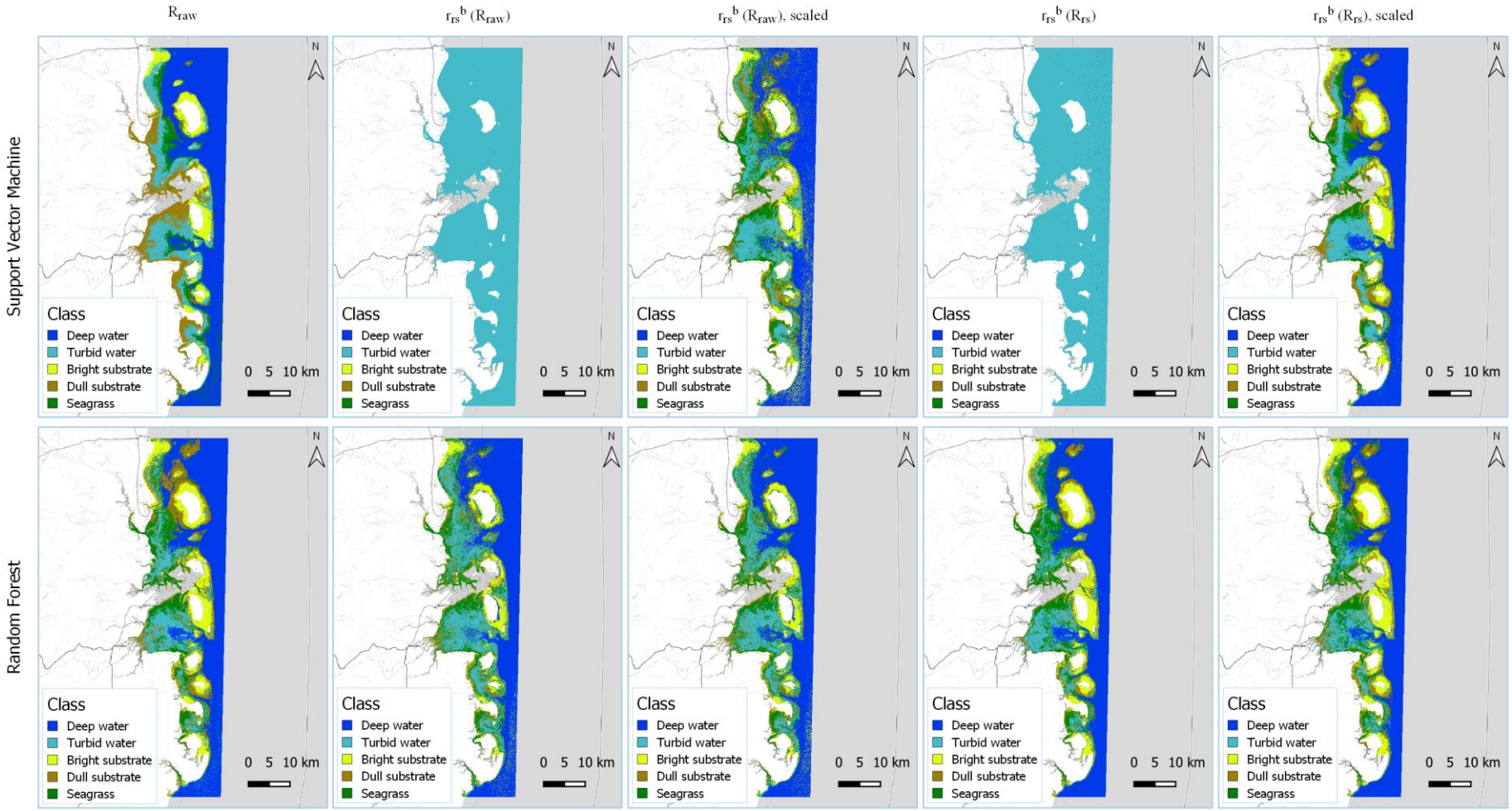

Figure 17. Overview of classification maps at QNP. The top row contains Support Vector Machine (SVM) maps and bottom Random Forest (RF) maps. The columns are in order of R_{raw}, R_{raw}-derived r_{rs}^b, scaled R_{raw}-derived r_{rs}^b, R_{rs}-derived r_{rs}^b and scaled R_{rs}-derived r_{rs}^b. Basemap: OpenTopoMap.

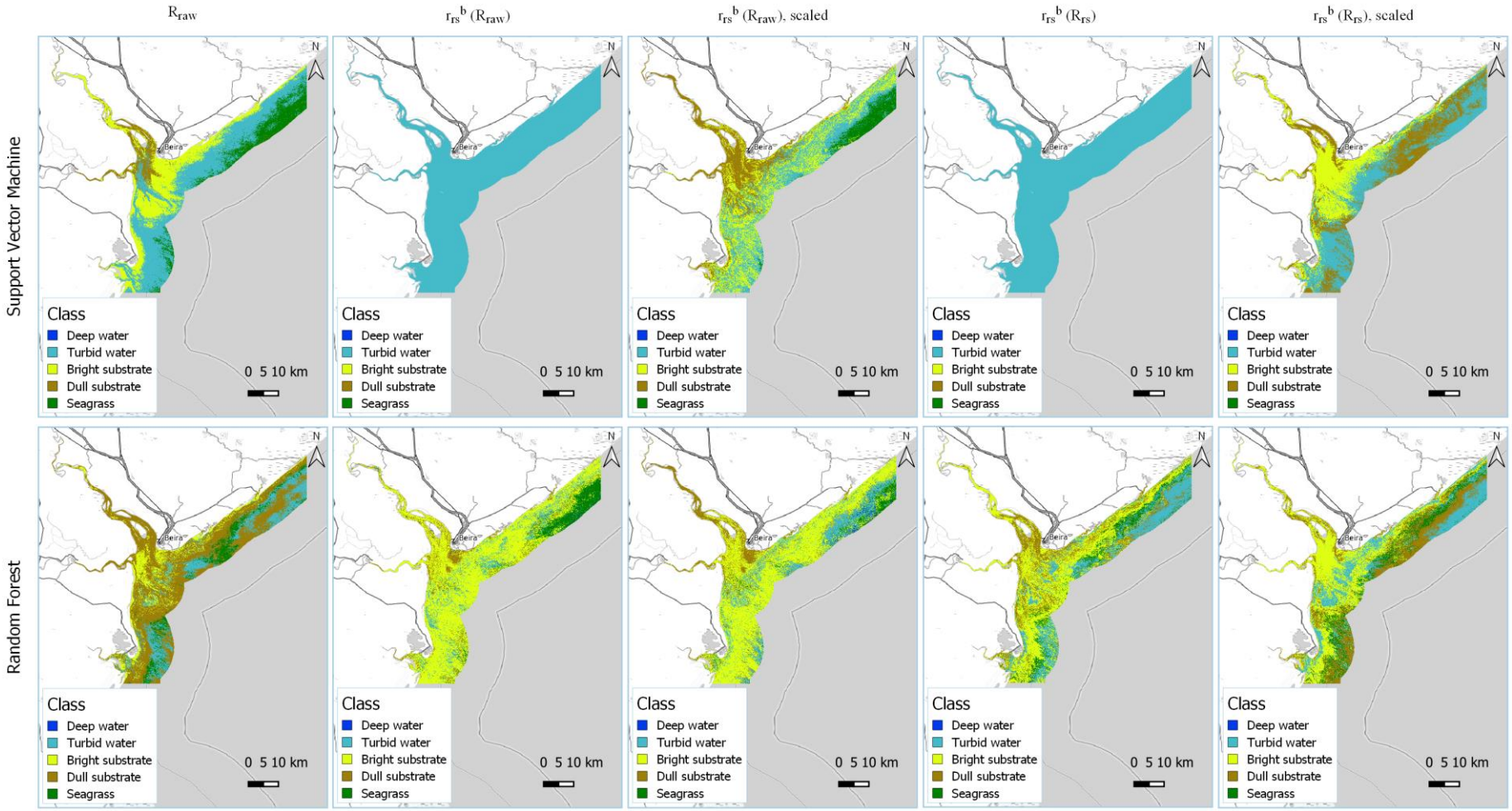

Figure 18. Overview of classification maps at Beira. The top row contains Support Vector Machine (SVM) maps and bottom Random Forest (RF) maps. The columns are in order of R_{raw}, R_{raw}-derived r_{rs}^{b}, scaled R_{raw}-derived r_{rs}^{b}, R_{rs}-derived r_{rs}^{b} and scaled R_{rs}-derived r_{rs}^{b}. Basemap: OpenTopoMap.

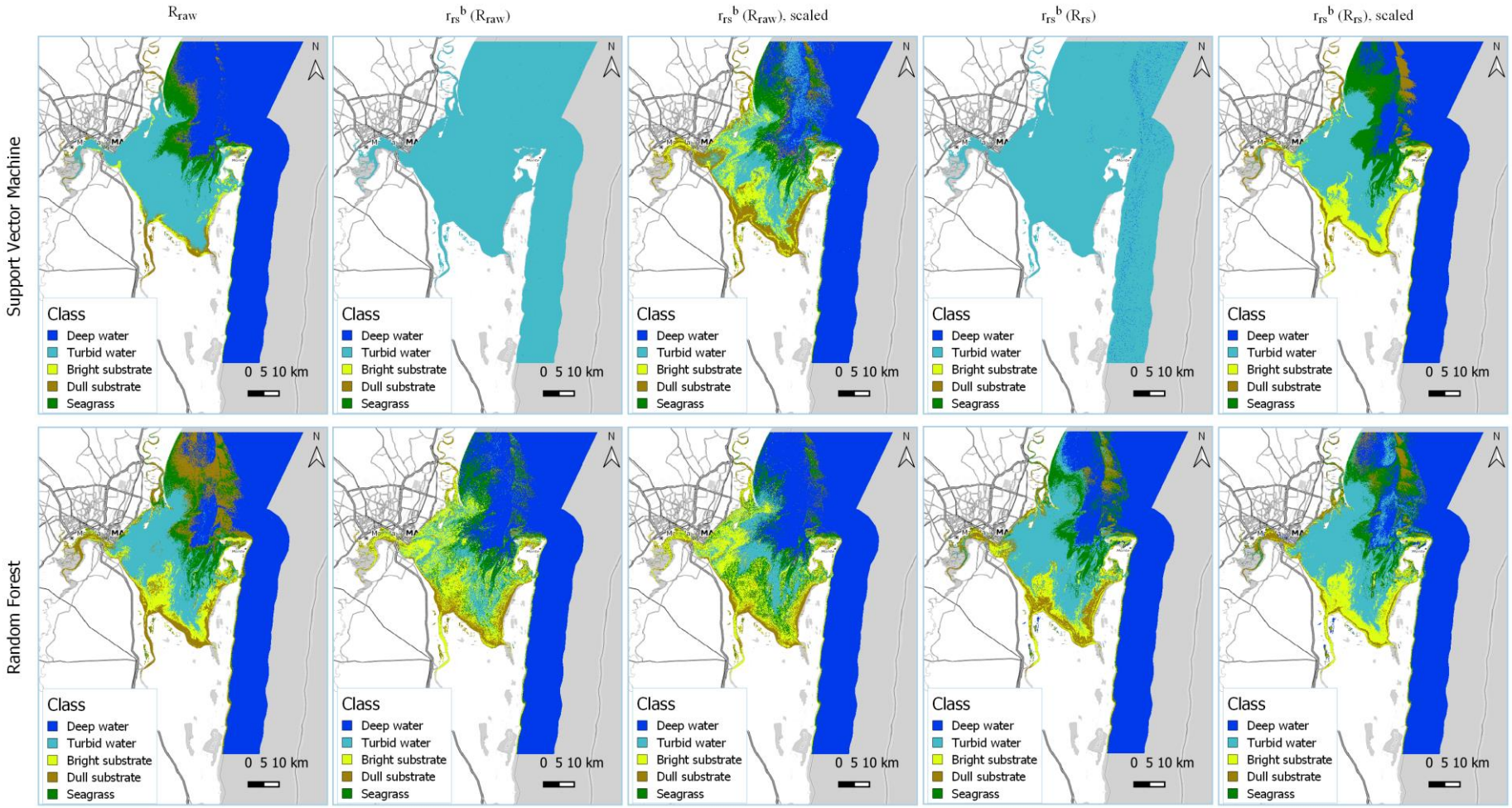

Figure 19. Overview of classification maps at Maputo. The top row contains Support Vector Machine (SVM) maps and bottom Random Forest (RF) maps. The columns are in order of R_{raw}, R_{raw}-derived r_{rs}^{b}, scaled R_{raw}-derived r_{rs}^{b}, R_{rs}-derived r_{rs}^{b} and scaled R_{rs}-derived r_{rs}^{b}. Basemap: OpenTopoMap.

On a local scale, RF maps outperform the SVM maps to accurately and precisely identify seagrasses. There were much more commissioning errors by the SVM maps, especially the best performing scaled R_{rs}-derived r_{rs}^b classification map. At Maputo, both the seaward (Figure 20) and inner bay seagrasses (Figure 21) were better identified using the RF maps. For the seaward seagrasses, the R_{raw} RF classification map was more fitting to the seagrass areas seen on the R_{raw} true colour composite than the r_{rs}^b RF classification maps (Figure 20). Some of the fringing seagrass areas were misidentified by SVM as turbid water areas, owing to the

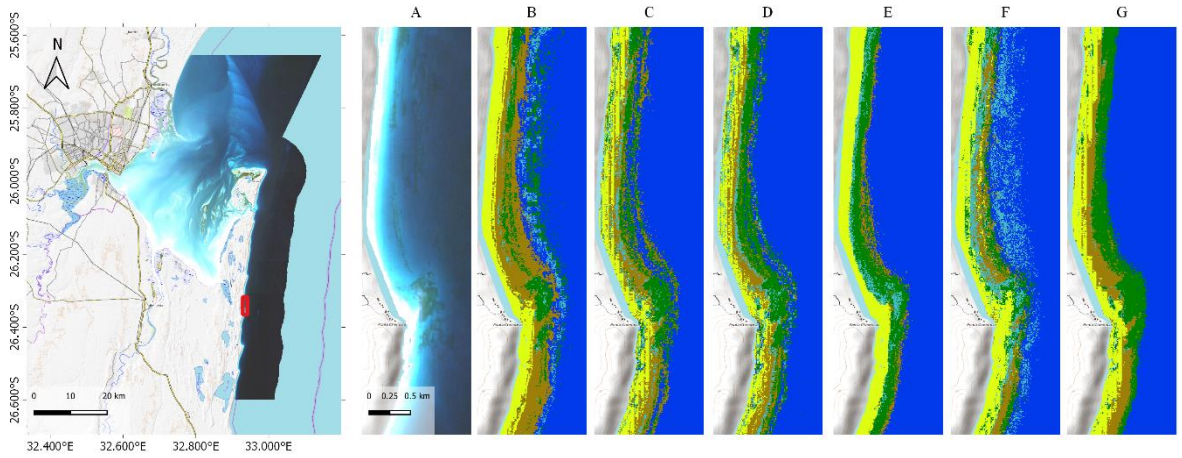

Figure 20. Close-up look at the performances of selected classification maps for the fringing seagrasses at Maputo (red inset box in the overview map). A: True colour composite of R_{raw}, B: R_{raw}, RF classification map, C: initial R_{rs}-derived r_{rs}^b, RF classification map, D: scaled R_{rs}-derived r_{rs}^b, RF classification map, E: R_{raw}, SVM classification map, F: scaled R_{raw}-derived r_{rs}^b, SVM classification map, G: scaled R_{rs}-derived r_{rs}^b, SVM classification map. These are the better performing maps for identifying the fringing seagrasses. The classification scheme is consistent with the overview maps Figure 17 – Figure 19. Basemap: OpenTopoMap.

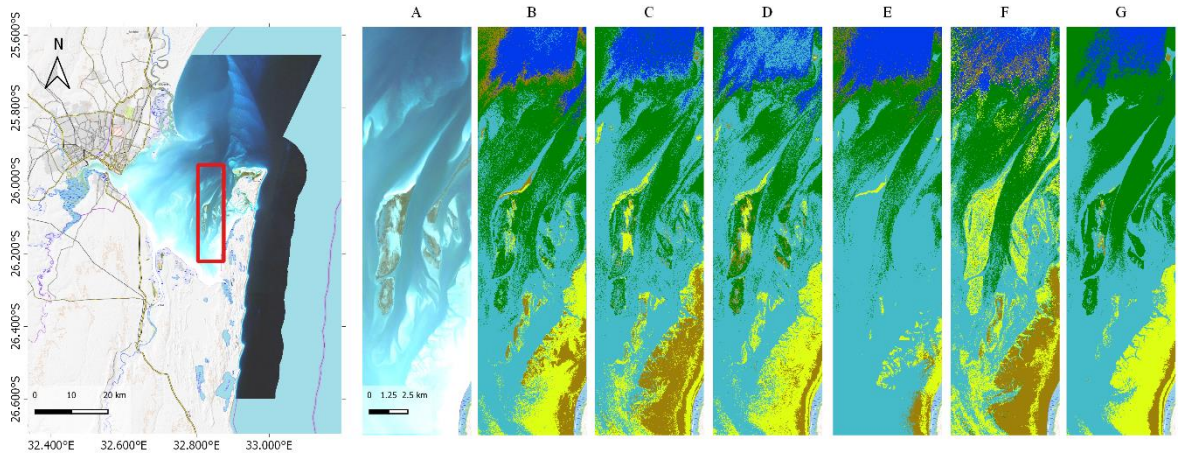

Figure 21. Close-up look at the performances of selected classification maps for the Inhaca island seagrasses at Maputo (red inset box in the overview map). A: True colour composite of R_{raw}, B: R_{raw}, RF classification map, C: initial R_{rs}-derived r_{rs}^b, RF classification map, D: scaled R_{rs}-derived r_{rs}^b, RF classification map, E: R_{raw}, SVM classification map, F: scaled R_{raw}-derived r_{rs}^b, SVM classification map, G: scaled R_{rs}-derived r_{rs}^b, SVM classification map. For comparison, the same classification maps were used as Figure 20. The classification scheme is consistent with the overview maps Figure 17 – Figure 19. Basemap: OpenTopoMap.

highly similar spectral nature between these two classes (Figure 16). The turbid water-seagrass class confusion was worse in the inner bay areas, with both the RF and SVM having the said issue and the addition of the bright substrate class to the confusion. This led to a worsened classification accuracy and grossly over-commissioned too many seagrass areas in the deeper, turbid water areas for all classification maps (Figure 21). The worst were the scaled R_{raw}-derived r_{rs}^{b} SVM classification map, which misidentified all seagrass areas as

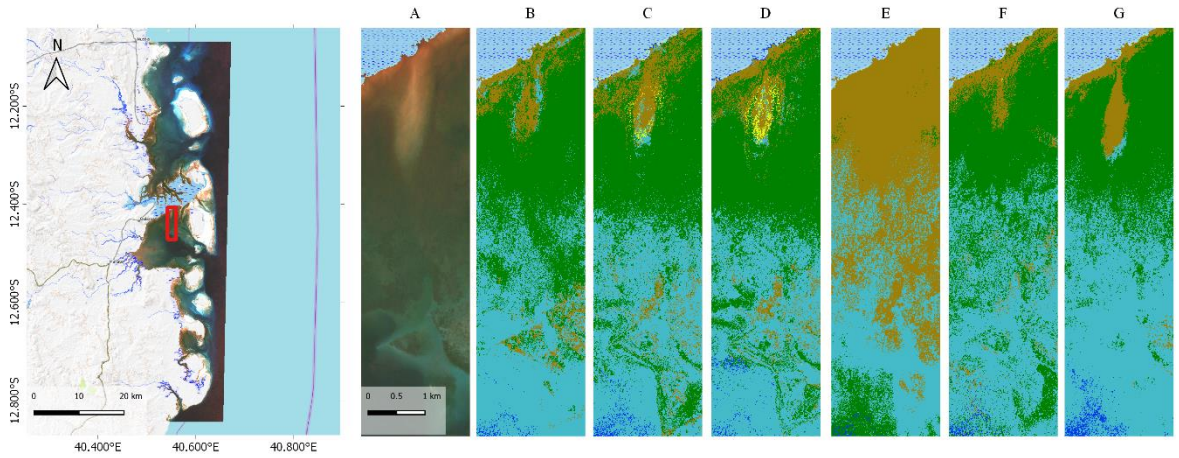

Figure 22. Close-up look at the performances of selected classification maps for the seagrasses on a mudflat at QNP (red inset box in the overview map). A: True colour composite of R_{raw}, B: R_{raw}, RF classification map, C: initial R_{rs}-derived r_{rs}^{b}, RF classification map, D: scaled R_{rs}-derived r_{rs}^{b}, RF classification map, E: R_{raw}, SVM classification map, F: scaled R_{raw}-derived r_{rs}^{b}, SVM classification map, G: scaled R_{rs}-derived r_{rs}^{b}, SVM classification map. For comparison, the same classification maps were used as Figure 20. The classification scheme is consistent with the overview maps Figure 17 – Figure 19. Basemap: OpenTopoMap.

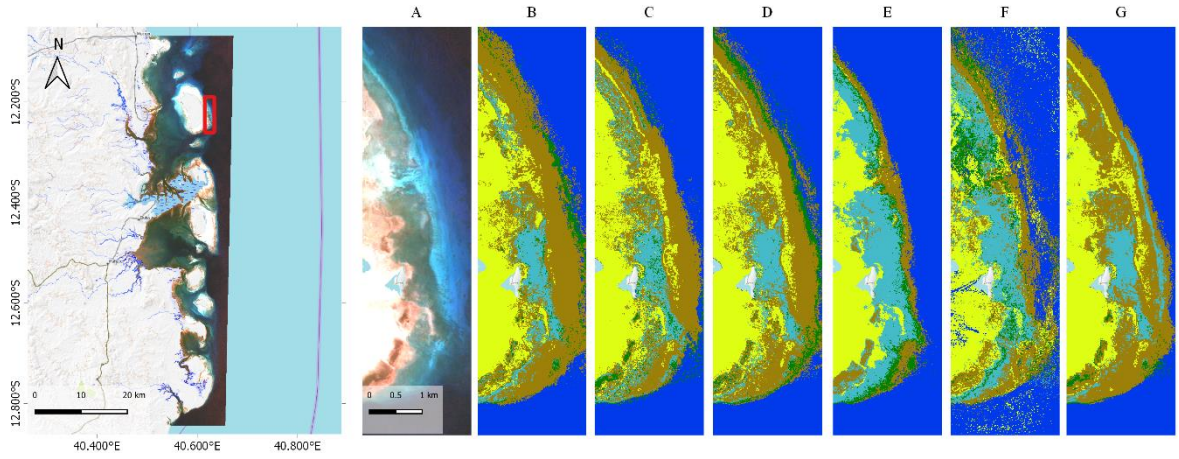

Figure 23. Close-up look at the performances of selected classification maps for the seagrasses at Matemo Island, QNP (red inset box in the overview map). A: True colour composite of R_{raw}, B: R_{raw}, RF classification map, C: initial R_{rs}-derived r_{rs}^{b}, RF classification map, D: scaled R_{rs}-derived r_{rs}^{b}, RF classification map, E: R_{raw}, SVM classification map, F: scaled R_{raw}-derived r_{rs}^{b}, SVM classification map, G: scaled R_{rs}-derived r_{rs}^{b}, SVM classification map. For comparison, the same classification maps were used as Figure 20. The classification scheme is consistent with the overview maps Figure 17 – Figure 19. Basemap: OpenTopoMap.

bright substrate and the surrounding deeper, turbid waters as seagrass instead, and the R_{raw} SVM classification map, which fully omitted the seagrass meadows of Inhaca Island as turbid water (Figure 21).

At QNP, the RF classification maps seemed to be able to better capture the seagrass patches further from the mangrove shoreline than SVM, with the R_{raw}-derived r_{rs}^{b} RF classification map being the closest to the perceivable seagrass meadows in the R_{raw} true colour composite (Figure 22). As mud is a duller substrate than sand, the seagrass-substrate class confusion here is with the dull substrate class, as compared to previously at the sandier Maputo. This is most evident with the R_{raw} SVM classification map which misidentifies the seagrass meadow in turbid waters as dull substrate. The SVM classifier was also unable to identify the deeper seagrass meadows in turbid waters in the southern half of Figure 22, with very few features of these meadows reflected in their output maps. For the seaward seagrass meadows in Figure 23, R_{rs}-derived r_{rs}^{b} RF classification map outlined the seagrass patches at Matemo Island best.

No local scale classification map inspection was performed at the Beira site, as no seagrass meadows were found at the site.

4.5. Estimated seagrass area

The resultant estimated seagrass area is influenced more by the input rather than its classifier, as the changing of the input such as R_{raw} versus r_{rs}^{b} as well as the scaling of r_{rs}^{b} (Table 7). The best SVM classification, the R_{rs}-derived r_{rs}^{b}, estimates the seagrass area to be 3518.37 km^2. Although the RF classifications generally have a similar overall accuracy (Table 6), their estimated seagrass area ranged from 3436.82 km^2 to 5033.44 km^2. Given the difference in areal estimates with between other input layers, it is indicative of an overprediction in seagrass areas beyond the training and validation data for both the initial and scaled R_{raw}-derived r_{rs}^{b}.

Table 7. Estimated seagrass area in square kilometres, based on the classification maps.

Classifier	R_{raw}	r_{rs}^{b} , R_{raw}-derived		r_{rs}^{b} , R_{rs}-derived	
		Initial	Scaled	Initial	Scaled
SVM	4219.22	6.67	5046.82	14.34	3518.37
RF	3576.61	5033.44	4955.40	3983.60	3436.82

5. Discussion

This study is an extension and combination of two seagrass studies in Greece, namely to implement a semi-analytical model on the cloud computing GEE platform (Traganos et al., 2018; Traganos & Reinartz, 2018). While it was a successful implementation of the semi-analytical model onto GEE to map seagrasses in Mozambique, there are new challenges to overcome. Unlike Greece and its Mediterranean waters, Mozambique is based in the open oceanic waters (Sete et al., 2002) and therefore has a different hydrology and environment which influence the detection of seagrass. It is essential to account for these regional conditions, regardless of a localised or global standardised approach. In line with its preceding studies, the results of this study contribute to the long-term aim of mapping the seagrass meadows throughout the world.

5.1. Performance of the implementation

5.1.1. Overestimation of meadow area

While the initial results serve as a starting estimate of the Mozambican seagrass, it is more likely to be an overestimate. Owing to optical limits of seagrass detection, it is highly possible for deeper subtidal seagrasses to be found in optically deep waters, thereby underestimating the distribution of seagrasses if they are present there. Even in optimal water conditions, Poursandis et al. (2019) found that the maximum optical limit in Greek waters was 32.2 m, although *Posidonia oceanica* can be found in deeper waters. However, there is a large overestimate of the shallow water seagrasses which most likely overly inflated the total area of the deeper water seagrasses. Thus, the areal estimates of this study are highly likely to be net overestimates.

Much of the overestimation is owing to the confusion between seagrass pixels and pixels of other dark pixel classes. Rather than a more specific, discriminating classification for fringing seagrasses, many of the better classification maps denote the whole thin stretch as seagrasses, which is wrong as the seagrasses are alternating with sandy substrate (Figure 17 – Figure 19). Furthermore, many dark pixels such as turbid and deep water classes have been misclassified as seagrasses and *vice versa* (Figure 16). This is a recurring issue for aquatic remote sensing – while bright and dark pixels are easily differentiated, the distinction between classes within each brightness category is not as clear (Klonowski, 2007). Klonowski (2007) found that the

darker seagrass and deep water classes tend to be mutually misclassified, as within brighter pixels such as sand and corals. It was with this approach that the training data for this study was also grouped into bright and dull substrate classes (Table 2). The general spectral differences between these classes (Figure 15) suggests that the classification would be worse if they had been aggregated into a single class. Similarly, the classes were further subdivided by the condition of the water, namely clear and turbid. This was in anticipation that the turbidity of the water would change the spectral information by severely reducing the contribution of the bottom to the overall spectral reflectance input (Hochberg et al., 2003). This is further supported by the spectral differences between these subclasses, within each relevant class (Figure 16). While the fine scale differentiation between dark pixels can still be further improved, the overall classification is still satisfactory on a national level.

5.1.2. Performance of GEE classifiers

SVM is sensitive to scaling as large scales may result in larger values dominating over smaller values and thus produce a different output (Hsu et al., 2003). This was also reflected in the study when scaling was needed in order to restrict the inflated r_{rs}^{b} reflectance values, despite preserving the proportional difference between pixels (Figure 13 & Figure 14). Shelestov et al. (2017) have also asserted that the SVM functions in GEE may not be functioning properly. On the other hand, RF is more susceptible to overfitting, especially for highly spatially autocorrelated datasets (Xiong et al., 2017). The dataset also needs to be balanced, as RF is biased towards any majority class, even if it is only 10% larger in size than the other classes (Millard & Richardson, 2015). Owing to the three different substrate types and the varying turbidity conditions across the whole Mozambican coastline, there were some difficulties in balancing all these subclasses (Table 2). Furthermore, RF is composed of binary decision trees that are still based on the values of the input data. As such, it was interesting for the quantitative overall accuracy of the RF classifier to be consistent regardless of input data (Table 6).

In general, it is more common for studies to export the results out of GEE for classification and analysis than to perform them in GEE. A common theme is that GEE either do not have the classifier that the study requires (Shelestov et al., 2017) or the classifiers do not perform as well as the same functions in another software (Anchang et al., 2020; Hird et al., 2017). While GEE classifiers are still useful, as Tsai et al. (2018) have shown with their overall

accuracy of over 70% for their land cover classification of the landscape at and around a nature reserve in China, the next natural step would be to use improved classification methods such as ensemble modelling or soft classification. Waske et al. (2010) have proven that an ensemble SVM method will outperform a conventional SVM or RF classifier as well as shown that classification accuracy will improve with more iterations. Meanwhile, Reschke & Hüttich (2014) have demonstrated the use of soft classification for wetlands, under which intertidal areas can be considered. Unfortunately, not only the classifier functions in GEE are very simplified and not as customisable (Hird et al., 2017), GEE's general preference for vectorisation over iterations also increases the technical difficulties of integrating more complex methods such as those previously mentioned. Regardless, attempts at integrating these custom methods into GEE should be done to fill this technical gap.

5.1.3. Performance of the different reflectance layers

As the influence of the water column has been removed, r_{rs}^{b} should be consistent across different biogeographic regions (Hochberg et al., 2004). This would have supposedly removed the need to perform a normalisation between different images before mosaicking, although its performance should be compared to the pseudoinvariant feature approach (Traganos et al., 2018). While the performance of r_{rs}^{b} products were better than the R_{raw} products for the SVM classifier (Table 5), the quantitative results for the RF classifier were similar (Table 6), providing inconsistent results. Regardless, it is obvious that a contributing factor to the weaker performance is the difference in performance between regions of different substrate types and environmental conditions. Classification was generally better at QNP (Figure 17) and weakest at the turbid, estuarine mud Beira (Figure 18). Hochberg et al. (2003) found that the contribution of the coral bottom reflectance decreases substantially in turbid waters as compared to clear waters. Not only would this be applicable to other bottom types, the very low contribution of the bottom would also affect its retrieval from only spectral values. Thus, it is likely that the turbid conditions at Beira and slightly more turbid conditions at Maputo might have weakened the classification performances. Further studies could investigate this matter, such as by adding more focus sites for each of the substrate types. Alternatively, this could be circumvented by classifying each region separately and then combining the final maps together.

Similarly, R_{raw} and R_{rs} have different implications in literature. The former is technically similar to a surface reflectance product for a terrestrial region while the latter only contains signals that have penetrated the water surface (Dierssen et al., 2019). This is based on the black pixel assumption whereby deep water pixels should not have any NIR signal since it should have been fully absorbed by the water column in deeper waters (Lee et al., 1998a; Siegel et al., 2000). However, Siegel et al. (2000) pointed out that this black pixel assumption is based on oligotrophic waters, and thus will overcorrect for turbid waters, implying that R_{rs} may underperform in the wrong aquatic conditions.

The R_{rs}-derived products from this study were generally better than the R_{raw}-derived products. Furthermore, the R_{rs} is mostly likely to better separate the seagrass class from other classes, as the seagrass class had a better spread of spectral values that only overlaps substantially with the turbid water class (Figure 16). Comparatively for the R_{raw} image, the seagrass class could be easily confused with the deep water and dull substrate class (Figure 15). While this comparison between R_{raw} and R_{rs} is seldom compared overtly in literature, many studies have reported success with using R_{rs} to detect seagrasses from other classes (Dierssen et al., 2019; Traganos & Reinartz, 2018). The omission of such comparison and focus on the use of R_{rs} may be interpreted as an affirmation to the use of R_{rs} over R_{raw}. Interestingly, the difference became negligible when the RF classifier was used. O'Neill et al. (2011) reported that the water column correction had overcorrected and overestimated the spectral values of their seagrass and deep sand classes deeper than 3 m, as the correction method is sensitive to the depth and downwelling attenuation coefficients. This is consistent with Siegel et al. (2000), who also discovered that the black pixel assumption would cause an overcorrection in the aerosol reflectance. Despite that and their low number of deeper seagrass samples, O'Neill et al. (2011) still had a high classification accuracy. Similarly, the Mozambican coastline have regions that are both turbid and clear. While this study used both R_{raw} and R_{rs} as an interim, it would be highly recommended to select one or implement a conditional black pixel correction for the more turbid waters (Siegel et al., 2000).

Unfortunately, no internal validation was designed for the IOP products in GEE. This is due to the complexity of various retrieval functions such as C2RCC (Brockmann et al., 2016) and inversion (Lee et al., 1998a) as well as the lack of ground truth data. As a substitute, an external validation was used, based on R_{rs} of a single scene. R_{raw} was not tested as there

were no issues for a single scene to undergo the standard HOPE model. Given the approximation nature of the total absorbance equation used here (Lee et al., 1998b), the difference in values with the C2RCC is acceptable. Nevertheless, it would still be better to enhance and implement a better approach to derive the total absorptance value as well as an internal validation for the IOP.

5.1.4. Satellite-derived Bathymetry (SDB)

The SDB estimates at Mozambique were satisfactory despite a low R^2, as a natural consequence of extrapolating from a geographically limited bathymetry dataset that is not fully representative of all the coasts of Mozambique (Green et al., 2003). Extrapolation from such a small representation would most likely produce inaccurate results (Waske et al., 2010). Furthermore, much of the data were collected within very shallow depths of 5 m or less. Although the refraction error when relating the optical imagery to the ground truth data would be low for such shallow depths (Parrish et al., 2019), this meant that the linear regression model used had to extrapolate for depths beyond 5 m. Also, the SDB estimation methods based on attenuation differences between the wavelengths of light in water column have an optimal working range, with the minimum depth determining the point whereby the attenuation differences are more noticeable and the maximum depth demarcating the point whereby too much light was lost to determine any such differences (Stumpf et al., 2003). The range has been estimated to be 5–10 m (Stumpf et al., 2003), 0–12 m (Pacheco et al., 2015) and 3–11 m (Klonowski, 2007). Finally, the collected data were from a boat survey and therefore were records of the water column depth. This meant that the negative depth values calculated were not equivalent to the mean sea level at chart datum as recorded in Sete et al. (2002), and thus a consistent underestimate. When considering the tidal range of QNP and Beira in conjunction with their mean sea levels (Sete et al., 2002), the negative depth estimates were still within the possible values. As an extension to these conclusions, the SDB result was systematically scaled and corrected into the positive range. While the available ground-truth bathymetry dataset is definitely not optimal, it is currently the only available data with high spatial resolution. If resources permit, more data from various other sites in Mozambique and over larger depth ranges could be collected to improve the SDB results.

The limited dataset is a large barrier to improving the SDB estimates. Unfortunately, there was no success in the search of other datasets. Radar-based datasets, such as the Shuttle

Radar Topography Mission (SRTM) and Advanced Land Observing Satellite (ALOS) global digital surface models (DSM), were limited by the low penetrative ability of radar wavelengths in water (DeVries et al., 2020). Meanwhile, the ETOPO1 dataset by the National Oceanic and Atmospheric Administration (NOAA) was too spatially coarse. It largely underestimated deeper waters and slightly overestimated shallower waters at Mozambique. Similarly, the spatial resolution of the General Bathymetric Chart of the Oceans (GEBCO) bathymetry dataset was also insufficient for this study. While the Ice, Cloud, and land Elevation Satellite-2 (ICESat-2) Bathymetry data shows much promise to provide high-resolution bathymetry data (Parrish et al., 2019), its bathymetry product is currently in development under a commercial firm and not yet available as of this report. Alternative methods in optical imagery such as using an SVM classification (Mishra et al., 2005), a band ratio method (Stumpf et al., 2003) and a look-up table (Dekker et al., 2011) all require good bathymetry data, which does not solve the issue. Li et al. (2019) modified the band ratio method to a data-agnostic equation. However, attempts to apply their method to derive the SDB in Mozambique failed. Furthermore, there are further challenges such as the implications of turbidity on an optically-derived SDB. The SDB estimates at Beira were bad (Figure 7) as the highly turbid waters were spectrally similar to the dull substrate classes (Figure 15). In spite of the initial failure to implement Li's methods and in face of the data deficiency in the region, a generalised or data-agnostic approach is the recommended direction for future scientific pursuits, although a campaign that involves much data collection would be the better solution.

5.2. Recurrent issues

5.2.1. Turbidity and optically deep pixels – "Unwanted" pixels in aquatic remote sensing

Turbidity and optically deep pixels are two major issues for aquatic remote sensing. The former causes optical obstruction which might be misidentified as a valid bottom cover (Figure 15 & Figure 16). Meanwhile, the latter has a very low signal return that may be misidentified as seagrass which has low returns too due to photosynthetic light absorption (Dierssen et al., 2019). Both issues affect all outputs of this study. Hossain et al. (2015) have also highlighted that turbidity reduces the accuracy of classification. It is difficult to identify and mask these pixels out despite the research efforts invested (Brando et al., 2009; Liu et al., 2019).

Turbidity may occur in a range of intensities (Liu et al., 2019). Regardless of intensity, a turbid area would have its spectral values affected by the turbid contributions to the signal (Hochberg et al., 2003). The greater the intensity, the less the contribution of bottom reflectance as light has less ability to penetrate through the water column (O'Neill et al., 2011) and thus the capability of the semi-analytical model to obtain an accurate bottom reflectance from that pixel. The current aquatic correction procedures are based on oligotrophic waters and will overcorrect turbid waters (Siegel et al., 2000). Furthermore, Whitlock et al. (1981) have discovered that turbid waters have different attenuation parameters that are slightly different from the standard models for aquatic remote sensing, which would implicate the retrieval of IOP values from these pixels. Using the HOPE model in conjunction with an airborne hyperspectral sensor, Dierssen et al. (2019) was able to correctly identify seagrass in the turbid water of Elkhorn Slough, California. While the HOPE model has been adapted to a multispectral system for seagrass detection (Traganos & Reinartz, 2018), our study was not as successful in detecting seagrasses in turbid waters. Alternatively, Dierssen et al. (2019) proposed a red edge detection method for shallow water seagrasses. Naturally, the loss of the ability to detect deeper seagrasses might not be a good trade-off at the seaward coasts of Mozambique. Siegel et al. (2000) proposed a modified black pixel correction for eutrophic waters, although they observed that not all turbid waters were due to eutrophication. As such, its applications will be limited for waters which turbidity arises from suspended inorganic particles rather than phytoplankton and other chlorophyll-containing particles. Other possible options include identifying turbid waters using indices or calculations and then masking them out like cloud pixels before image composition (Liu et al., 2019).

While optically deep waters will naturally cover a range of water depths, spectrally these pixels are supposed to be very low in spectral signal and highly similar, especially when assuming the water column is homogeneous (Lyzenga, 1978). This means that the optically deep pixels can be distinguished from the optically shallow waters with a threshold and then masked out to better aid the classification. By adapting from Maritorena et al. (1994), O'Neill et al. (2011) used a semi-analytical equation to determine the maximum water depth of shallow waters by calculating an index from known deep water pixels. Similarly, Brando et al. (2009) used an index measuring the contribution of bottom reflectance to identify optically deep waters, based on an advanced HOPE model. The former method is reliant on prior

knowledge of known deep waters while the latter is both based on inversion as well as highly scene dependent. As such, the former method might be easier to adapt to GEE, without any consideration of the GEE usage quota for now. While most conventional approaches are more focussed on using reflectance values to identify optically deep waters (Gege, 2014), a reverse approach can also be taken by focussing on the attenuation index of each pixel and then comparing them to the attenuation index values of optically deep pixels. If these values are highly similar, then it can be easily quantified if these tested pixels are optically deep pixels too. This method would be highly advantageous in regions with a heterogeneous IOP throughout the image, as well as address the aforementioned assumption that the water column is homogeneous and therefore can be subjected to the same IOP models or equations.

5.2.2. Limitations of GEE

While GEE performs very well in bulk geospatial processing (Mutanga & Kumar, 2019; Shelestov et al., 2017), its power is curbed by anti-abuse or anti-overload measures, namely the usage quota (Gorelick et al., 2017). The ramifications of this quota extend beyond a simple adaptation and implementation of any existing scientific methods onto the GEE platform.

Multi-image composition is an approach that is highly recommended in order to manage the size of the data and its computational demands (Carrasco et al., 2019). The most common application is to create a multitemporal composite, which is also used to resolve issues such as noise, cloud cover, cloud shadows, sun glint and even missing data (Amani et al., 2019; Shelestov et al., 2017; Traganos et al., 2018). Hird et al. (2017) proposed that the statistical approach of the composite filters out anomalous or extreme values, which are generally associated with the bright cloud or dark shadow pixels. When working in the frequently cloudy tropical region of Southeast Asia, Oliphant et al. (2019) relied on interannual multitemporal images of Moderate-resolution Imaging Spectroradiometer (MODIS) to remove any cloud pixels from their images. While a similar effect was experienced for many of the regions in Mozambique, the normalisation of pixels was not as successful in Beira, as in its final classification product (Figure 18). Perhaps owing to the high turbidity all year round, the statistical representative of many of the pixels were of the highly turbid waters instead. Furthermore, cloud shadows were still noted in the composite, likely due to the inconsistency in the number of cloud-free occurrences over time for each pixel within the area (Carrasco et al., 2019). Increasing the percentile used for the statistical composition would have led to the

introduction of sun-glinted waters in other areas. This strongly indicates that the statistical normalisation of an image composite may not be completely effective in resolving these issues. A possible solution is to use the image metadata to filter out images with lower solar and viewing angles, as images with higher solar and viewing angles would be more likely to have their cloud pixels overlapping their respective shadows. The trade-off for this solution is the reduction in number of relevant images, which may affect the statistical representative per pixel (Carrasco et al., 2019). Conventional local server data cubes or other cloud computing platforms such as Amazon Web Services (AWS) could also be used as an alternative, although the former would most likely require much local storage and processing memories while the latter provides its services at a cost (Sugumaran et al., 2018).

There are also two other issues of image composition that are specific to the semi-analytical approach, namely the lack of a true metadata and the artificial relationship between pixels spatially and spectrally. The artificial spectral and spatial relationship between pixels is not the issue *per se*, as this also occurs during inversion on a lesser scale. The values of each pixel are tuned after every iteration cycle of the optimisation to fit the provided equations. Fortunately, the issues of optimisation, such as multiple valid sets of results owing to multiple local minima or maxima or the need to input valid starting values (Gege, 2014; Klonowski, 2007), does not pertain to the image composition approach. The bottom reflectance formula in Equation (5) indicates that the solar zenith angle and the sensor look angle are essential components of the equation. However, after compositing different images with different metadata together, there are no applicable metadata for the artificial image. It is compounded by the second issue of GEE executing the statistical reduction separately by band, so a pixel in one spectral band may originate from an image with different angles as the "same" pixel in another spectral band. This study followed the assumption of its predecessor in Greece to assume a nadir sensor angle (Traganos & Reinartz, 2018). Meanwhile, a mean solar zenith angle of all valid images was used as a substitute. While the alternative is to filter the images and limit them to a narrower range of angles, this will reduce the number of usable images and consequently reduce the effectiveness of the image composition approach (Carrasco et al., 2019). Another implication of the second issue is that the slightly different, artificial relationship within pixels spectrally may result in overcorrection when applying the semi-analytical equations. For example, the correction from R_{raw} to R_{rs} relies on using the

SWIR band to remove the influence of the atmosphere from the signal. If the return pixel for the SWIR band happens to be slightly higher than the other bands, then an overcorrection would occur, causing issues with the subsequent calculations. Currently, a counter-correction was done by rescaling the values in a standardised manner, which reduces the amount of subjectivity introduced during the choice of scaling.

In order to successfully perform a classification in GEE, the total number of training data should not exceed 1 million pixels (Amani et al., 2019). This study found that GEE converts polygon training data into points per pixel in the polygon, thereby inflating any training data based on polygons. In turn, this would increase the chances of exceeding the usage quota. Therefore, any polygons in the training data should be similar in size as well as small, in order to both balance the training data per class as well as ensure that the usage quota is not exceeded. Alternatively, as done by this study, training points can be taken. However, the selection of training points is more delicate than of polygons, as representation of both edges and centre might need to be done, depending on classifier (Millard & Richardson, 2015). While mapping Canadian wetlands on a national level, Amani et al. (2019) have also discovered that the certain classifiers as well as certain tuning parameters of the classifiers in GEE are more computationally demanding, which in turn lowers the size threshold for the training data. The lowered number of training data would definitely impact the overall classification accuracy (Millard & Richardson, 2015). Shelestov et al. (2017) observed that the GEE classifiers did not perform as well as other software, while other studies have pointed out the inadequacy of GEE classifiers (Anchang et al., 2020; Hird et al., 2017). All these indicate that the classification procedure in GEE still requires further improvement.

5.3. Future work

Many studies are starting to exploit the processing power of GEE performing their study end-to-end on the platform GEE (Amani et al., 2019; Koskinen et al., 2019; Oliphant et al., 2019). Still, there are other studies that rely on GEE only as a very powerful image pre-processor before exporting the data (Anchang et al., 2020; Hird et al., 2017). Despite its limitations, GEE is generally user-friendly to both geospatial specialists and non-specialists, save for a low coding barrier of entry (Alonso et al., 2016; Koskinen et al., 2019; Oliphant et al., 2019). It hosts a wide catalogue of datasets which can be combined in many different ways (Carrasco et al., 2019; Wu et al., 2019). Its end-to-end service from data to analysis

circumvents issues with huge data download and management when processing geospatial information on larger spatial and temporal scales (Anchang et al., 2020; Gorelick et al., 2017). Furthermore, once a procedure is set up in GEE, it is highly automated and can be transferred and scaled to other regions, depending on the design (Anchang et al., 2020; Wu et al., 2019). Since GEE is under continuous development and will further improve, it has great potential to bridge geospatial applications with other scientific fields. The development of the various global habitat maps for use by the wider scientific and management audience further supports this (Hansen et al., 2013; Murray et al., 2019; Pekel et al., 2016).

Moving forward, while the results of this study are acceptable for a pilot study for the region, there is still a need for improvement in order to achieve its long-term aims. An inaccurate monitoring system is worse than not having a monitoring system, as it would provide false security with its inaccurate information (Schultz et al., 2015). This false security is highly damaging, both on a scientific and management front, as managers and policy makers would not have the correct information and thus focus other on critical issues instead. Therefore, it is highly recommended to further improve the semi-analytical model for seagrass detection and increase its accuracy.

Beyond Mozambique, tropical regions such as Southeast Asia are rich in seagrass diversity (Fortes et al., 2018) and have a high cloud frequency and cover (Oliphant et al., 2019). Although radar remote sensing can penetrate clouds to provide a surface image (Carrasco et al., 2019), its lack of penetrative ability through the water surface limits its application here (DeVries et al., 2020). The higher temporal resolution MODIS could be used to cover the issue of cloud cover at a trade-off to spatial resolution (Alonso et al., 2016), which also suggests the possibility of using Landsat optical imagery as an alternative. Per as previous global land cover maps in GEE, the availability of many satellite imagery archives allows for retroactive monitoring, as well as up-to-date with the continued ingestion of the most recent images onto the GEE platform (Murray et al., 2019; Pekel et al., 2016), including analyses such as real-time change detection (Koskinen et al., 2019). Pertaining to aquatic remote sensing, other analytical models could be explored to further improve the detection of seagrasses, such as the more advanced Bottom Reflectance Unmixing Computation of the Environment (BRUCE) and Semi-analytical Model for Bathymetry, Unmixing, and Concentration Assessment (SAMBUCA) models that are built on HOPE or the various look up table

approaches (Dekker et al., 2011), provided that these methods are able to fit within the GEE usage quota. Alternative approaches could also be investigated, such as using the spectral reflectance profile of water to estimate another coastal aerosol band B0 for Sentinel-2 for more classification features (Wei et al., 2019). All these will contribute to the larger goal of mapping the global distribution of subtidal seagrass meadows.

6. Conclusion

This study implemented the semi-analytical HOPE model onto GEE to map seagrasses in Mozambique successfully. It was able to produce an area estimate of seagrasses in Mozambique, as well as the SDB and IOP products. However, there are new challenges to overcome.

The best estimate of the seagrass area in Mozambique is 3518.37 km^2, based on a seagrass producer's accuracy of 51.02%, a seagrass user's accuracy of 65.79% and an overall classification accuracy of 60.27% by the scaled R_{rs}-derived SVM classification map, which is relatively good for a regional scale classification. It is highly likely that the areal estimate is an overestimate due to commissioning. The SVM classifier had the best overall accuracy while the RF classifier had a more consistent performance. SVM classification maps were also less noisy than RF classification maps, but seemed to be less sensitive to finer changes between neighbouring pixels. Classification using different intermediate and final images of the semi-analytical model also shed more light to the importance of each processing step, such as the black pixel assumption and the need to scale the r_{rs}^b reflectance values before performing an SVM classification. The most direct approach to improve the classification accuracies is to supplement more ground truth data.

The SDB and IOP estimates were side products of this modelling. Despite the limited amount of ground truth data available, the best SDB estimate was based on the R_{raw} and able to achieve an R^2 of 0.68. SDB estimates were qualitatively satisfactory at QNP and Maputo, but bad in Beira due to the highly turbid waters. The upcoming ICESat-2 bathymetry product might also be potentially useful as ground truth data for the SDB estimation. Meanwhile, there is current no internal validation for the IOP. However, external validation suggested that the approximation equations are a sufficient substitute for the more complex C2RCC processing algorithm.

Regardless of products, the general effects of turbidity, misidentification of deep water class with other classes, as well as the GEE usage quota applied to all. Turbidity is a major issue at Beira, owing to the large reliance of the HOPE model, the SDB estimation and the IOP approximation on optical imagery processing. Furthermore, many of the aquatic remote sensing equations are designed based on clear waters rather than turbid waters, thus these

processes are not sufficiently suited for highly turbid waters. Meanwhile, for the deep water pixels, their low signal returns or dark pixels cause them to be easily misidentified as seagrasses or other dark pixel classes. Nonetheless, there exist possible solutions to resolve these issues of turbid waters and deep waters, which need to be further investigated and adapted for this study. For the usage quota, it is a restriction that needs to be accounted for when selecting GEE as the geospatial processing platform of choice. Despite its enforced limitations, GEE has proven to be a very powerful platform for large scale geospatial data management, processing and analysis. Should the usage quota of GEE pose a big deterrent, other data cubes as well as cloud computing services such as AWS could serve as possible alternatives.

While more work is required to refine the seagrass detection algorithm using a semi-analytical model, its semi-analytical approach has shown potential to detect seagrass meadows, especially for remote or understudied regions with few prior data available. The transferability of this approach is also shown as it was originally implemented in Greece and its Mediterranean waters. This is highly advantageous since the approach could easily be implemented in another region of the world, albeit with some adaptation to the local climate and hydrology. The results of this study will contribute to producing a global seagrass classification map, which is highly relevant and much needed to the fields of seagrass science and conservation management.

7. Reference

Alonso, A., Muñoz-Carpena, R., Kennedy, R.E., & Murcia, C., 2016. Wetland landscape spatio-temporal degradation dynamics using the new google earth engine cloud-based platform: Opportunities for non-specialists in remote sensing. Trans. ASABE 59, 1333–1344. https://doi.org/10.13031/trans.59.11608

Amani, M., Mahdavi, S., Afshar, M., Brisco, B., Huang, W., Mirzadeh, S.M.J., White, L., Banks, S., Montgomery, J., & Hopkinson, C., 2019. Canadian wetland inventory using Google Earth Engine: The first map and preliminary results. Remote Sens. 11, 1–20. https://doi.org/10.3390/RS11070842

Anchang, J.Y., Prihodko, L., Ji, W., Kumar, S.S., Ross, C.W., Yu, Q., Lind, B., Sarr, M.A., Diouf, A.A., & Hanan, N.P., 2020. Toward Operational Mapping of Woody Canopy Cover in Tropical Savannas Using Google Earth Engine. Front. Environ. Sci. 8. https://doi.org/10.3389/fenvs.2020.00004

Arias-Ortiz, A., Serrano, O., Masqué, P., Lavery, P.S., Mueller, U., Kendrick, G.A., Rozaimi, M., Esteban, A., Fourqurean, J.W., Marbà, N., Mateo, M.A., Murray, K., Rule, M.J., & Duarte, C.M., 2018. A marine heatwave drives massive losses from the world's largest seagrass carbon stocks. Nat. Clim. Chang. 1–7. https://doi.org/10.1038/s41558-018-0096-y

Austin, R.W., & Petzold, T.J., 1986. Spectral dependence of the diffuse attenuation coefficient of light in ocean waters.

Austin, R.W., & Petzold, T.J., 1981. The Determination of the Diffuse Attenuation Coefficient of Sea Water using the Coastal Zone Color Scanner.

Bandeira, S., & Björk, M., 2001. Seagrass research in the eastern Africa region: Emphasis on diversity, ecology and ecophysiology. South African J. Bot. 67, 420–425. https://doi.org/10.1016/S0254-6299(15)31158-3

Bandeira, S., Gullstrom, M., Balidy, H., Samussone, D., & Cossa, D., 2014. Seagrass meadows in Maputo Bay, in: The Maputo Bay Ecosystem. pp. 147–186.

Bostater, C.R., & Rotkiske, T., 2018. Influence of bottom depths and bottom types on water surface reflectance. SPIE-Intl Soc Optical Eng, p. 45. https://doi.org/10.1117/12.2515669

Brando, V.E., Anstee, J.M., Wettle, M., Dekker, A.G., Phinn, S.R., & Roelfsema, C., 2009. A physics based retrieval and quality assessment of bathymetry from suboptimal hyperspectral data. Remote Sens. Environ. 113, 755–770. https://doi.org/10.1016/j.rse.2008.12.003

Bricaud, A., Babin, M., Morel, A., & Claustre, H., 1995. Variability in the chlorophyll-specific absorption coefficients of natural phytoplankton: Analysis and parameterization. J. Geophys. Res. 100, 13321. https://doi.org/10.1029/95JC00463

Bricaud, A., Morel, A., & Prieur, L., 1981. Absorption by dissolved organic matter of the sea (yellow substance) in the UV and visible domains', Limnol. Oceanogr.

Brockmann, C., Doerffer, R., Peters, M., Stelzer, K., Embacher, S., & Ruescas, A., 2016. Evolution of the C2RCC neural network for Sentinel 2 and 3 for the retrieval of ocean colour products in normal and extreme optically complex waters, in: European Space Agency, (Special Publication) ESA SP. European Space Agency.

Caballero, I., & Stumpf, R.P., 2019. Retrieval of nearshore bathymetry from Sentinel-2A and 2B satellites in South Florida coastal waters. Estuar. Coast. Shelf Sci. 226. https://doi.org/10.1016/j.ecss.2019.106277

Canhanga, S., & Dias, J.M., 2005. Tidal characteristics of Maputo Bay, Mozambique. J. Mar. Syst. 58, 83–97. https://doi.org/10.1016/j.jmarsys.2005.08.001

Carrasco, L., O'Neil, A.W., Daniel Morton, R., & Rowland, C.S., 2019. Evaluating combinations of temporally aggregated Sentinel-1, Sentinel-2 and Landsat 8 for land cover mapping with Google Earth Engine. Remote Sens. 11. https://doi.org/10.3390/rs11030288

Cooper, J.A.G., & Pilkey, O.H., 2002. The Barrier Islands of Southern Mozambique. J. Coast. Res. 36, 164–172. https://doi.org/10.2112/1551-5036-36.sp1.164

Davidson, N.C., Van Dam, A.A., Finlayson, C.M., & McInnes, R.J., 2019. Worth of wetlands: Revised global monetary values of coastal and inland wetland ecosystem services. Mar. Freshw. Res. https://doi.org/10.1071/MF18391

de los Santos, C.B., Krause-Jensen, D., Alcoverro, T., Marbà, N., Duarte, C.M., van Katwijk, M.M., Pérez, M., Romero, J., Sánchez-Lizaso, J.L., Roca, G., Jankowska, E., Pérez-Lloréns,

J.L., Fournier, J., Montefalcone, M., Pergent, G., Ruiz, J.M., Cabaço, S., Cook, K., Wilkes, R.J., Moy, F.E., Trayter, G.M.-R., Arañó, X.S., de Jong, D.J., Fernández-Torquemada, Y., Auby, I., Vergara, J.J., & Santos, R., 2019. Recent trend reversal for declining European seagrass meadows. Nat. Commun. https://doi.org/10.1038/s41467-019-11340-4

Dekker, A.G., Phinn, S.R., Anstee, J., Bissett, P., Brando, V.E., Casey, B., Fearns, P., Hedley, J., Klonowski, W., Lee, Z.P., Lynch, M., Lyons, M., Mobley, C., & Roelfsema, C., 2011. Intercomparison of shallow water bathymetry, hydro-optics, and benthos mapping techniques in Australian and Caribbean coastal environments. Limnol. Oceanogr. Methods 9, 396–425.

DeVries, B., Huang, C., Armston, J., Huang, W., Jones, J.W., & Lang, M.W., 2020. Rapid and robust monitoring of flood events using Sentinel-1 and Landsat data on the Google Earth Engine. Remote Sens. Environ. 240, 111664. https://doi.org/10.1016/j.rse.2020.111664

Dierssen, H.M., Bostrom, K.J., Chlus, A., Hammerstrom, K., Thompson, D.R., & Lee, Z., 2019. Pushing the Limits of Seagrass Remote Sensing in the Turbid Waters of Elkhorn Slough, California. Remote Sens. 11, 1664. https://doi.org/10.3390/rs11141664

Duarte, C.M., 2002. The future of seagrass meadows. Environ. Conserv. 29, 192–206. https://doi.org/10.1017/S0376892902000127

Duarte, C.M., & Cebrián, J., 1996. The fate of marine autotrophic production. Limnol. Oceanogr. 41, 1758–1766. https://doi.org/10.4319/lo.1996.41.8.1758

Duarte, C.M., Dennison, W.C., Orth, R.J.W., & Carruthers, T.J.B., 2008. The charisma of coastal ecosystems: Addressing the imbalance. Estuaries and Coasts 31, 233–238. https://doi.org/10.1007/s12237-008-9038-7

Duffy, J.E., Benedetti-Cecchi, L., Trinanes, J., Muller-Karger, F.E., Ambo-Rappe, R., Boström, C., Buschmann, A.H., Byrnes, J., Coles, R.G., Creed, J., Cullen-Unsworth, L.C., Diaz-Pulido, G., Duarte, C.M., Edgar, G.J., Fortes, M., Goni, G., Hu, C., Huang, X., Hurd, C.L., Johnson, C., Konar, B., Krause-Jensen, D., Krumhansl, K., Macreadie, P., Marsh, H., McKenzie, L.J., Mieszkowska, N., Miloslavich, P., Montes, E., Nakaoka, M., Norderhaug, K.M., Norlund, L.M., Orth, R.J., Prathep, A., Putman, N.F., Samper-Villarreal, J., Serrao, E.A., Short, F., Pinto, I.S., Steinberg, P., Stuart-Smith, R., Unsworth, R.K.F., van Keulen, M., van

Tussenbroek, B.I., Wang, M., Waycott, M., Weatherdon, L. V., Wernberg, T., & Yaakub, S.M., 2019. Toward a coordinated global observing system for seagrasses and marine macroalgae. Front. Mar. Sci. 6. https://doi.org/10.3389/fmars.2019.00317

Esteban, N., Unsworth, R.K.F., Gourlay, J.B.Q., & Hays, G.C., 2018. The discovery of deep-water seagrass meadows in a pristine Indian Ocean wilderness revealed by tracking green turtles. Mar. Pollut. Bull. 134, 99–105. https://doi.org/10.1016/j.marpolbul.2018.03.018

Evans, S.M., Griffin, K.J., Blick, R.A.J., Poore, A.G.B., & Vergés, A., 2018. Seagrass on the brink: Decline of threatened seagrass posidonia australis continues following protection. PLoS One 13. https://doi.org/10.1371/journal.pone.0190370

Figueiredo, I.N., Pinto, L., & Gonçalves, G., 2016. A modified Lyzenga's model for multispectral bathymetry using Tikhonov regularization. IEEE Geosci. Remote Sens. Lett. 13, 53–57. https://doi.org/10.1109/LGRS.2015.2496401

Flanders Marine Institute, 2019. MarineRegions.org [WWW Document]. URL www.marineregions.org (accessed 11.8.19).

Fortes, M.D., 2018. Seagrass ecosystem conservation in Southeast Asia needs to link science to policy and practice. Ocean Coast. Manag. 159, 51–56. https://doi.org/10.1016/j.ocecoaman.2018.01.028

Fortes, M.D., Ooi, J.L.S., Tan, Y.M., Prathep, A., Bujang, J.S., & Yaakub, S.M., 2018. Seagrass in Southeast Asia: A review of status and knowledge gaps, and a road map for conservation. Bot. Mar. https://doi.org/10.1515/bot-2018-0008

Gege, P., 2014. WASI-2D: A software tool for regionally optimized analysis of imaging spectrometer data from deep and shallow waters. Comput. Geosci. 62, 208–215. https://doi.org/10.1016/j.cageo.2013.07.022

Gordon, H.R., & Morel, A.Y., 1983. Remote Assessment of Ocean Color for Interpretation of Satellite Visible Imagery. A Review, Lecture Notes on Coastal and Estuarine Studies., Springer-Verlag, New York.

Gorelick, N., Hancher, M., Dixon, M., Ilyushchenko, S., Thau, D., & Moore, R., 2017. Google Earth Engine: Planetary-scale geospatial analysis for everyone. Remote Sens. Environ.

202, 18–27. https://doi.org/10.1016/j.rse.2017.06.031

Grech, A., Chartrand-Miller, K., Erftemeijer, P., Fonseca, M., McKenzie, L., Rasheed, M., Taylor, H., & Coles, R., 2012. A comparison of threats, vulnerabilities and management approaches in global seagrass bioregions. Environ. Res. Lett. 7. https://doi.org/10.1088/1748-9326/7/2/024006

Green, E.P., Short, F.T., & Frederick, T., 2003. World atlas of seagrasses. Univ of California Press.

Hansen, M.C., Potapov, P. V., Moore, R., Hancher, M., Turubanova, S.A., Tyukavina, A., Thau, D., Stehman, S. V., Goetz, S.J., Loveland, T.R., Kommareddy, A., Egorov, A., Chini, L., Justice, C.O., & Townshend, J.R.G., 2013. High-resolution global maps of 21st-century forest cover change. Science (80-.). https://doi.org/10.1126/science.1244693

Hedley, J., Russell, B., Randolph, K., & Dierssen, H., 2016. A physics-based method for the remote sensing of seagrasses. Remote Sens. Environ. 174, 134–147. https://doi.org/10.1016/j.rse.2015.12.001

Hird, J.N., DeLancey, E.R., McDermid, G.J., & Kariyeva, J., 2017. Google Earth Engine, open-access satellite data, and machine learning in support of large-area probabilistic wetland mapping. Remote Sens. 9. https://doi.org/10.3390/rs9121315

Hochberg, E.J., Atkinson, M.J., & Andréfouët, S., 2003. Spectral reflectance of coral reef bottom-types worldwide and implications for coral reef remote sensing. Remote Sens. Environ. 85, 159–173. https://doi.org/10.1016/S0034-4257(02)00201-8

Hochberg, E.J., Atkinson, M.J., Apprill, A., & Andréfouët, S., 2004. Spectral reflectance of coral. Coral Reefs 23, 84–95. https://doi.org/10.1007/s00338-003-0350-1

Hossain, M.S., Bujang, J.S., Zakaria, M.H., & Hashim, M., 2015. The application of remote sensing to seagrass ecosystems: an overview and future research prospects. Int. J. Remote Sens. https://doi.org/10.1080/01431161.2014.990649

Hsu, C.-W., Chang, C.-C., & Lin, C.-J., 2003. A Practical Guide to Support Vector Classification.

Jackson, E.L., Rees, S.E., Wilding, C., & Attrill, M.J., 2015. Use of a seagrass residency index to apportion commercial fishery landing values and recreation fisheries expenditure to

seagrass habitat service. Conserv. Biol. 29, 899–909. https://doi.org/10.1111/cobi.12436

Kerr, J.M., & Purkis, S., 2018. An algorithm for optically-deriving water depth from multispectral imagery in coral reef landscapes in the absence of ground-truth data. Remote Sens. Environ. 210, 307–324. https://doi.org/10.1016/j.rse.2018.03.024

Kirk, J.T.O., 1984. Attenuation of solar radiation in scattering–absorbing waters: a simplified procedure for its calculation. Appl. Opt. 23, 3737. https://doi.org/10.1364/ao.23.003737

Klonowski, W.M., 2007. Retrieving key benthic cover types and bathymetry from hyperspectral imagery. J. Appl. Remote Sens. 1, 011505. https://doi.org/10.1117/1.2816113

Koedsin, W., Intararuang, W., Ritchie, R.J., & Huete, A., 2016. An integrated field and remote sensing method for mapping seagrass species, cover, and biomass in Southern Thailand. Remote Sens. 8. https://doi.org/10.3390/rs8040292

Koskinen, J., Leinonen, U., Vollrath, A., Ortmann, A., Lindquist, E., d'Annunzio, R., Pekkarinen, A., & Käyhkö, N., 2019. Participatory mapping of forest plantations with Open Foris and Google Earth Engine. ISPRS J. Photogramm. Remote Sens. 148, 63–74. https://doi.org/10.1016/j.isprsjprs.2018.12.011

Kovacs, E., Roelfsema, C., Lyons, M., Zhao, S., & Phinn, S., 2018. Seagrass habitat mapping: How do landsat 8 OLI, sentinel-2, ZY-3A, and worldview-3 perform? Remote Sens. Lett. 9, 686–695. https://doi.org/10.1080/2150704X.2018.1468101

Kumar, L., & Mutanga, O., 2018. Google Earth Engine applications since inception: Usage, trends, and potential. Remote Sens. 10. https://doi.org/10.3390/rs10101509

Lee, Z., 1994. Visible-Infrared Remote-Sensing Model and Applications for Ocean Waters.

Lee, Z., Carder, K.L., & Arnone, R.A., 2002. Deriving inherent optical properties from water color: a multiband quasi-analytical algorithm for optically deep waters. Appl. Opt. 41, 5755. https://doi.org/10.1364/ao.41.005755

Lee, Z., Carder, K.L., Chen, R.F., & Peacock, T.G., 2001. Properties of the water column and bottom derived from Airborne Visible Infrared Imaging Spectrometer (AVIRIS) data. J. Geophys. Res. Ocean. 106, 11639–11651. https://doi.org/10.1029/2000jc000554

Lee, Z., Carder, K.L., Mobley, C.D., Steward, R.G., & Patch, J.S., 1999. Hyperspectral remote sensing for shallow waters: 2 Deriving bottom depths and water properties by optimization. Appl. Opt. 38, 3831. https://doi.org/10.1364/ao.38.003831

Lee, Z., Carder, K.L., Mobley, C.D., Steward, R.G., & Patch, J.S., 1998a. Hyperspectral remote sensing for shallow waters I A semianalytical model. Appl. Opt. 37, 6329. https://doi.org/10.1364/ao.37.006329

Lee, Z., Carder, K.L., Steward, R.G., Peacock, T.G., Davis, C.O., & Patch, J.S., 1998b. An empirical algorithm for light absorption by ocean water based on color. J. Geophys. Res. Ocean. 103, 22967–22978. https://doi.org/10.1029/98JC01946

Li, J., Knapp, D.E., Schill, S.R., Roelfsema, C., Phinn, S., Silman, M., Mascaro, J., & Asner, G.P., 2019. Adaptive bathymetry estimation for shallow coastal waters using Planet Dove satellites. Remote Sens. Environ. 232. https://doi.org/10.1016/j.rse.2019.111302

Ligi, M., Kutser, T., Kallio, K., Attila, J., Koponen, S., Paavel, B., Soomets, T., & Reinart, A., 2017. Testing the performance of empirical remote sensing algorithms in the Baltic Sea waters with modelled and in situ reflectance data. Oceanologia 59, 57–68. https://doi.org/10.1016/j.oceano.2016.08.002

Liu, H., Hu, S., Zhou, Q., Li, Q., & Wu, G., 2019. Revisiting effectiveness of turbidity index for the switching scheme of NIR-SWIR combined ocean color atmospheric correction algorithm. Int. J. Appl. Earth Obs. Geoinf. 76, 1–9. https://doi.org/10.1016/j.jag.2018.10.010

Luisetti, T., Jackson, E.L., & Turner, R.K., 2013. Valuing the European “coastal blue carbon” storage benefit. Mar. Pollut. Bull. 71, 101–106. https://doi.org/10.1016/j.marpolbul.2013.03.029

Lyzenga, D.R., 1985. Shallow-water bathymetry using combined lidar and passive multispectral scanner data. Int. J. Remote Sens. 6, 115–125. https://doi.org/10.1080/01431168508948428

Lyzenga, D.R., 1981. Remote sensing of bottom reflectance and water attenuation parameters in shallow water using aircraft and landsat data. Int. J. Remote Sens. 2, 71–82. https://doi.org/10.1080/01431168108948342

Lyzenga, D.R., 1978. Passive remote sensing techniques for mapping water depth and bottom features.

Lyzenga, D.R., Malinas, N.P., & Tanis, F.J., 2006. Multispectral bathymetry using a simple physically based algorithm. IEEE Trans. Geosci. Remote Sens. 44, 2251–2259. https://doi.org/10.1109/TGRS.2006.872909

Maritorena, S., Morel, A., & Gentili, B., 1994. Diffuse reflectance of oceanic shallow waters: Influence of water depth and bottom albedo. Limnol. Oceanogr. 39, 1689–1703. https://doi.org/10.4319/lo.1994.39.7.1689

Markull, K., Lencart e Silva, J.D., Simpson, J.H., & Dias, J.M., 2014. The influence of the Maputo and Incomati rivers on the mixing and outflow of freshwater from Maputo Bay (Mozambique). J. Coast. Res. 70, 580–585. https://doi.org/10.2112/si70-098.1

Millard, K., & Richardson, M., 2015. On the importance of training data sample selection in Random Forest image classification: A case study in peatland ecosystem mapping. Remote Sens. 7, 8489–8515. https://doi.org/10.3390/rs70708489

Mishra, D.R., Narumalani, S., Rundquist, D., & Lawson, M., 2005. High-resolution ocean color remote sensing of benthic habitats: A case study at the Roatan Island, Honduras. IEEE Trans. Geosci. Remote Sens. 43, 1592–1603. https://doi.org/10.1109/TGRS.2005.847790

Misra, A., Vojinovic, Z., Ramakrishnan, B., Luijendijk, A., & Ranasinghe, R., 2018. Shallow water bathymetry mapping using Support Vector Machine (SVM) technique and multispectral imagery. Int. J. Remote Sens. 39, 4431–4450. https://doi.org/10.1080/01431161.2017.1421796

Mobley, C.D., Stramski, D., Bissett, W.P., & Boss, E., 2004. Optical Modeling of Ocean Waters: Is the Case 1-Case 2 Classification Still Useful? Oceanography.

Morel, A., 1974. Optical properties of pure water and pure sea water, in: Jerlov, N.G., & Nielsen, E.S. (Eds.), Optical Aspects of Oceanography. Academic Press, pp. 1–24.

Murray, N.J., Phinn, S.R., DeWitt, M., Ferrari, R., Johnston, R., Lyons, M.B., Clinton, N., Thau, D., & Fuller, R.A., 2019. The global distribution and trajectory of tidal flats. Nature.

https://doi.org/10.1038/s41586-018-0805-8

Mutanga, O., & Kumar, L., 2019. Google earth engine applications. Remote Sens. https://doi.org/10.3390/rs11050591

Nakaoka, M., & Aioi, K., 1999. Growth of seagrass Halophila ovalis at dugong trails compared to existing within-patch variation in a Thailand intertidal flat. Mar. Ecol. Prog. Ser. 184, 97–103. https://doi.org/10.3354/meps184097

Nordlund, L.M., Koch, E.W., Barbier, E.B., & Creed, J.C., 2016. Seagrass ecosystem services and their variability across genera and geographical regions. PLoS One 11. https://doi.org/10.1371/journal.pone.0163091

O'Neill, J.D., Costa, M., & Sharma, T., 2011. Remote sensing of shallow coastal benthic substrates: In situ spectra and mapping of eelgrass (Zostera marina) in the Gulf Islands National Park Reserve of Canada. Remote Sens. 3, 975–1005. https://doi.org/10.3390/rs3050975

Odermatt, D., Gitelson, A., Brando, V.E., & Schaepman, M., 2012. Review of constituent retrieval in optically deep and complex waters from satellite imagery. Remote Sens. Environ. https://doi.org/10.1016/j.rse.2011.11.013

Oliphant, A.J., Thenkabail, P.S., Teluguntla, P., Xiong, J., Gumma, M.K., Congalton, R.G., & Yadav, K., 2019. Mapping cropland extent of Southeast and Northeast Asia using multi-year time-series Landsat 30-m data using a random forest classifier on the Google Earth Engine Cloud. Int. J. Appl. Earth Obs. Geoinf. 81, 110–124. https://doi.org/10.1016/j.jag.2018.11.014

Pacheco, A., Horta, J., Loureiro, C., & Ferreira, 2015. Retrieval of nearshore bathymetry from Landsat 8 images: A tool for coastal monitoring in shallow waters. Remote Sens. Environ. 159, 102–116. https://doi.org/10.1016/j.rse.2014.12.004

Parrish, C.E., Magruder, L.A., Neuenschwander, A.L., Forfinski-Sarkozi, N., Alonzo, M., & Jasinski, M., 2019. Validation of ICESat-2 ATLAS bathymetry and analysis of ATLAS's bathymetric mapping performance. Remote Sens. 11. https://doi.org/10.3390/rs11141634

Pekel, J.F., Cottam, A., Gorelick, N., & Belward, A.S., 2016. High-resolution mapping of global surface water and its long-term changes. Nature. https://doi.org/10.1038/nature20584

Phinn, S., Roelfsema, C., Kovacs, E., Canto, R., Lyons, M., Saunders, M., & Maxwell, P., 2018. Mapping, monitoring and modelling seagrass using remote sensing techniques, in: Seagrasses of Australia: Structure, Ecology and Conservation. Springer International Publishing, pp. 445–487. https://doi.org/10.1007/978-3-319-71354-0_15

Poursanidis, D., Traganos, D., Reinartz, P., & Chrysoulakis, N., 2019. On the use of Sentinel-2 for coastal habitat mapping and satellite-derived bathymetry estimation using downscaled coastal aerosol band. Int. J. Appl. Earth Obs. Geoinf. 80, 58–70. https://doi.org/10.1016/j.jag.2019.03.012

Preen, A., 1995. Impacts of dugong foraging on seagrass habitats: observational and experimental evidence for cultivation grazing. Mar. Ecol. Prog. Ser. 124, 201–213. https://doi.org/10.3354/meps124201

Purvaja, R., Robin, R.S., Ganguly, D., Hariharan, G., Singh, G., Raghuraman, R., & Ramesh, R., 2018. Seagrass meadows as proxy for assessment of ecosystem health. Ocean Coast. Manag. 159, 34–45. https://doi.org/10.1016/j.ocecoaman.2017.11.026

Reschke, J., & Hüttich, C., 2014. Continuous field mapping of Mediterranean wetlands using sub-pixel spectral signatures and multi-temporal Landsat data. Int. J. Appl. Earth Obs. Geoinf. 28, 220–229. https://doi.org/10.1016/j.jag.2013.12.014

Roelfsema, C.M., Lyons, M., Kovacs, E.M., Maxwell, P., Saunders, M.I., Samper-Villarreal, J., & Phinn, S.R., 2014. Multi-temporal mapping of seagrass cover, species and biomass: A semi-automated object based image analysis approach. Remote Sens. Environ. 150, 172–187. https://doi.org/10.1016/j.rse.2014.05.001

Schultz, S.T., Kruschel, C., Bakran-Petricioli, T., & Petricioli, D., 2015. Error, power, and blind sentinels: The statistics of seagrass monitoring. PLoS One 10. https://doi.org/10.1371/journal.pone.0138378

Sete, C., Ruby, J., & Dove, V., 2002. Seasonal variation of tides, currents, salinity and temperature along the coast of Mozambique.

Shelestov, A., Lavreniuk, M., Kussul, N., Novikov, A., & Skakun, S., 2017. Exploring Google Earth Engine platform for big data processing: Classification of multi-temporal satellite imagery for crop mapping. Front. Earth Sci. 5, 1–10. https://doi.org/10.3389/feart.2017.00017

Sheppard, J.K., Lawler, I.R., & Marsh, H., 2007. Seagrass as pasture for seacows: Landscape-level dugong habitat evaluation. Estuar. Coast. Shelf Sci. 71, 117–132. https://doi.org/10.1016/j.ecss.2006.07.006

Siegel, D.A., Wang, M., Maritorena, S., & Robinson, W., 2000. Atmospheric correction of satellite ocean color imagery: the black pixel assumption. Appl. Opt. 39, 3582. https://doi.org/10.1364/ao.39.003582

Sosik, H., 2008. Characterizing seawater constituents from optical properties. op. cit.,UNESCO, pp. 281-32 281–329.

Stumpf, R.P., Holderied, K., & Sinclair, M., 2003. Determination of water depth with high-resolution satellite imagery over variable bottom types, Limnol. Oceanogr.

Su, H., Liu, H., & Heyman, W., 2008. Automated derivation of bathymetric information from multi-spectral satellite imagery using a non-linear inversion model, in: Marine Geodesy. https://doi.org/10.1080/01490410802466652

Su, L., & Huang, Y., 2019. Seagrass resource assessment using World View-2 imagery in the Redfish Bay, Texas. J. Mar. Sci. Eng. 7. https://doi.org/10.3390/jmse7040098

Sugumaran, R., Hegeman, J.W., Sardeshmukh, V.B., & Armstrong, M.P., 2018. Processing remote-sensing data in cloud computing environments, in: Thenkabail, P.S. (Ed.), Remote Sensing Handbook-Three Volume Set. CRC Press, pp. 587–596. https://doi.org/10.1201/b19294

Topouzelis, K., Makri, D., Stoupas, N., Papakonstantinou, A., & Katsanevakis, S., 2018. Seagrass mapping in Greek territorial waters using Landsat-8 satellite images. Int. J. Appl. Earth Obs. Geoinf. 67, 98–113. https://doi.org/10.1016/j.jag.2017.12.013

Traganos, D., Aggarwal, B., Poursanidis, D., Topouzelis, K., Chrysoulakis, N., & Reinartz, P., 2018. Towards global-scale seagrass mapping and monitoring using Sentinel-2 on Google

Earth Engine: The case study of the Aegean and Ionian Seas. Remote Sens. 10. https://doi.org/10.3390/rs10081227

Traganos, D., & Reinartz, P., 2018. Machine learning-based retrieval of benthic reflectance and Posidonia oceanica seagrass extent using a semi-analytical inversion of Sentinel-2 satellite data. Int. J. Remote Sens. 39, 9428–9452. https://doi.org/10.1080/01431161.2018.1519289

Tsai, Y.H., Stow, D., Chen, H.L., Lewison, R., An, L., & Shi, L., 2018. Mapping vegetation and land use types in Fanjingshan National Nature Reserve using Google Earth Engine. Remote Sens. 10. https://doi.org/10.3390/rs10060927

Tyllianakis, E., Callaway, A., Vanstaen, K., & Luisetti, T., 2019. The value of information: Realising the economic benefits of mapping seagrass meadows in the British Virgin Islands. Sci. Total Environ. 650, 2107–2116. https://doi.org/10.1016/j.scitotenv.2018.09.296

UNEP-WCMC; Frederick T Short, 2017. Global Distribution of Seagrasses (version 6.0).

Unsworth, R.K.F., Ambo-Rappe, R., Jones, B.L., La Nafie, Y.A., Irawan, A., Hernawan, U.E., Moore, A.M., & Cullen-Unsworth, L.C., 2018. Indonesia's globally significant seagrass meadows are under widespread threat. Sci. Total Environ. 634, 279–286. https://doi.org/10.1016/j.scitotenv.2018.03.315

Unsworth, R.K.F., McKenzie, L.J., Collier, C.J., Cullen-Unsworth, L.C., Duarte, C.M., Eklöf, J.S., Jarvis, J.C., Jones, B.L., & Nordlund, L.M., 2019a. Global challenges for seagrass conservation. Ambio 48, 801–815. https://doi.org/10.1007/s13280-018-1115-y

Unsworth, R.K.F., Nordlund, L.M., & Cullen-Unsworth, L.C., 2019b. Seagrass meadows support global fisheries production. Conserv. Lett. 12. https://doi.org/10.1111/conl.12566

Waske, B., Van Der Linden, S., Benediktsson, J.A., Rabe, A., & Hostert, P., 2010. Sensitivity of support vector machines to random feature selection in classification of hyperspectral data. IEEE Trans. Geosci. Remote Sens. 48, 2880–2889. https://doi.org/10.1109/TGRS.2010.2041784

Waycott, M., Duarte, C.M., Carruthers, T.J.B., Orth, R.J., Dennison, W.C., Olyarnik, S., Calladine,

A., Fourqurean, J.W., Heck, K.L., Hughes, A.R., Kendrick, G.A., Kenworthy, W.J., Short, F.T., & Williams, S.L., 2009. Accelerating loss of seagrasses across the globe threatens coastal ecosystems. Proc. Natl. Acad. Sci. U. S. A. 106, 12377–12381. https://doi.org/10.1073/pnas.0905620106

Wei, J., Lee, Z., Shang, S., & Yu, X., 2019. Semianalytical Derivation of Phytoplankton, CDOM, and Detritus Absorption Coefficients From the Landsat 8/OLI Reflectance in Coastal Waters. J. Geophys. Res. Ocean. https://doi.org/10.1029/2019JC015125

Whitlock, C.H., Poole, L.R., Usry, J.W., Houghton, W.M., Witte, W.G., Morris, W.D., & Gurganus, E.A., 1981. Comparison of reflectance with backscatter and absorption parameters for turbid waters. Appl. Opt. 20, 517. https://doi.org/10.1364/ao.20.000517

Wicaksono, P., Fauzan, M.A., Kumara, I.S.W., Yogyantoro, R.N., Lazuardi, W., & Zhafarina, Z., 2019. Analysis of reflectance spectra of tropical seagrass species and their value for mapping using multispectral satellite images. Int. J. Remote Sens. https://doi.org/10.1080/01431161.2019.1624866

Wicaksono, P., & Lazuardi, W., 2018. Assessment of PlanetScope images for benthic habitat and seagrass species mapping in a complex optically shallow water environment. Int. J. Remote Sens. 39, 5739–5765. https://doi.org/10.1080/01431161.2018.1506951

Wu, Q., Lane, C.R., Li, X., Zhao, K., Zhou, Y., Clinton, N., DeVries, B., Golden, H.E., & Lang, M.W., 2019. Integrating LiDAR data and multi-temporal aerial imagery to map wetland inundation dynamics using Google Earth Engine. Remote Sens. Environ. 228, 1–13. https://doi.org/10.1016/j.rse.2019.04.015

Xiong, J., Thenkabail, P.S., Tilton, J.C., Gumma, M.K., Teluguntla, P., Oliphant, A., Congalton, R.G., Yadav, K., & Gorelick, N., 2017. Nominal 30-m cropland extent map of continental Africa by integrating pixel-based and object-based algorithms using Sentinel-2 and Landsat-8 data on Google Earth Engine. Remote Sens. 9. https://doi.org/10.3390/rs9101065

Yang, D., & Yang, C., 2009. Detection of seagrass distribution changes from 1991 to 2006 in Xincun Bay, Hainan, with satellite remote sensing. Sensors 9, 830–844. https://doi.org/10.3390/s90200830

York, P.H., Smith, T.M., Coles, R.G., McKenna, S.A., Connolly, R.M., Irving, A.D., Jackson, E.L., McMahon, K., Runcie, J.W., Sherman, C.D.H., Sullivan, B.K., Trevathan-Tackett, S.M., Brodersen, K.E., Carter, A.B., Ewers, C.J., Lavery, P.S., Roelfsema, C.M., Sinclair, E.A., Strydom, S., Tanner, J.E., van Dijk, K. jent, Warry, F.Y., Waycott, M., & Whitehead, S., 2017. Identifying knowledge gaps in seagrass research and management: An Australian perspective. Mar. Environ. Res. https://doi.org/10.1016/j.marenvres.2016.06.006

Zhang, X., & Hu, L., 2009. Scattering by pure seawater at high salinity. Opt. Express 17, 12685. https://doi.org/10.1364/oe.17.012685